Crystal organisation and material properties of *Chama* and *Glycymeris* myostraca and shells

S. Hoerl [a,*], T. le Moine [a], N.J. Peter [b], S. Amini [c], E. Griesshaber [a], J. Wang [b], E.M. Harper [d], C. Salas [e], A.G. Checa [f,g], R. Schwaiger [b], W.W. Schmahl [a]

[a] Department of Geo- and Environmental Sciences, Ludwig-Maximilians-Universität München, Munich, Germany
[b] IEK-2: Microstructure and Properties of Materials, Forschungszentrum Jülich GmbH, Institute of Energy and Climate Research, Jülich, Germany
[c] Department of Biomaterials, Max Planck Institute of Colloids and Interfaces, Potsdam, Germany
[d] Department of Earth Sciences, University of Cambridge, Downing Street, Cambridge CB2 3EQ, UK
[e] Departamento Biología Animal, Facultad de Ciencias, Universidad de Málaga, Málaga, Spain
[f] Instituto Andaluz de Ciencias de la Tierra, CSIC-Universidad de Granada, Armilla, Spain
[g] Departamento de Estratigrafía y Paleontología, Universidad de Granada, Granada, Spain

ARTICLE INFO

ABSTRACT

Movement of bivalve hard and soft tissue requires muscular action. Despite diverse bivalve lifestyles and living environments, the myostracum, a specific hard tissue formed where muscles attach to the shell, appears similar in structure for species of many bivalve orders.

We investigated myostracal and non-myostracal, valve, microstructure, texture and material properties of Chamidae and Glycymerididae species with electron-backscatter-diffraction, laser-confocal and backscatter electron imaging and nanoindentation testing. Chamidae and Glycymerididae follow different lifestyles and live in distinct environments. Chamidae are cemented to substrate and live in wave-swept, shallow, waters. Glycymerididae dwell in calm water and burrow into sandy/muddy sediment.

We found that myostracal aragonite of all investigated species has a crystal assembly pattern that reflects crystal growth through growth competition. Aragonite is extensively twinned in the myostracum and non-myostracal, valve, layers, not in the calcitic ornamentation. For myostracal aragonite, we found cyclic twinning, for non-myostracal aragonite the twinning was polysynthetic or polycyclic. We show how twinning and crystallographic texture are transmitted between myostracal and non-myostracal, valve, layers. Relative to non-biological aragonite, myostracal and non-myostracal, valve, indentation elastic modulus is reduced by 10–15 % and 15–20 %, respectively; myostracal and valve hardness is increased by 15–20 % and 5–10 %, respectively. Comparing modulus and hardness between aragonitic microstructures, we found that, relative to other microstructures, myostracal modulus is increased by 5 % and myostracal hardness by 15 %. Hence, the myostracal material shows a unique and specific microstructure, texture, modulus, and hardness that might be necessary for muscle attachment to enable the lifestyle-controlled requirements posed onto the organism.

1. Introduction

Biomineralized tissues are important for understanding the relationship between crystal organisation and properties of materials (e.g. [1–4]). Through hundreds of millions of years of natural selection, organisms developed targeted hard- and soft-tissue microstructures and fabrics for purposes such as adherence, motion, locomotion, vision, protection and many more. Called forth by many different lifestyles, derived adaptations of biomaterials were the consequence. These enabled survival in a wide range of habitats (e.g. [5–7]).

Of particular interest are the hard tissues of shelled organisms, e.g. molluscs and brachiopods. These are, in most cases, multi-layered and the different shell layers have different modes of crystal organisation. Deciphering the arrangement pattern of the crystals and understanding their formation mechanism is of main interest, not only for understanding the diversity of biomaterial generation principles but also as a source of information for the construction of man-made materials with targeted tissue properties [8–14].

Bivalve shells consist of calcium carbonate crystals that are embedded into an organic matrix of proteins, lipids and polysaccharides. Depending on the shell structure, the fraction of organic substance varies in proportion to the total shell weight (usually 0.1–5 mass%) and amino acid composition [15–17]. Bivalve shells often comprise both main carbonate polymorphs, aragonite and calcite, however, never mix them in a single morphological type of shell microstructure. The most widespread bivalve shell microstructure is the crossed-lamellar arrangement of aragonite biocrystals. The nacreous and columnar crystal assemblies are often utilized, but significantly less widespread. Due to the mode of crystal and organic substance organisation, the latter three microstructures are well known for their ability to stop crack development and progression and to promote crack deflection within the hard tissue [18–21].

Bivalves attach their mantle and organs to the shell via muscles: the foot attaches with the pedal, the mantle with the pallial and adductor, and the gill with the retractor muscles [22]. At muscle attachment sites a specific layer of carbonate crystals is deposited, referred to as the myostracum. The latter consists solely of aragonite and has a prominent microstructure and texture that is distinct from the other layers of the shell [23–27]. Myostraca can be found within the shell, between the inner and outer shell layers, or as patches along the inner shell surface.

The overall aim of the study presented here is to describe and discuss valve and myostracum microstructures, textures and material property characteristics for Chamidae (order Venerida) and Glycymerididae (order Arcida) shells. We choose animals that belong to different bivalve genera, form thick, but differently-sized shells, live in different habitats and follow distinct lifestyles. *Glycymeris* and *Chama* are abundant in many seas and oceans [28,29]. *Glycymeris* forms large aragonitic shells [30,31] that can reach more than 10 cm in diameter [32]. Glycymerididae live in turbid, calm, fairly shallow marine environments (up to 200 m) and use their siphonal openings and valves to burrow into the sediment [33,34]. With their circular shape and lack of a functional byssus, the shells are perfectly adapted for anterior-posterior rocking locomotion, which is the mode of movement used to traverse the substrate [30,34,35]. Chamidae are found in warm, tidal, wave-swept marine environments and live within the upper 30 m of the water column [36]. *Chama* bivalves are sedentary; for protection, they form thick, aragonitic, circular shells that are 3–5 cm in diameter [37,38]. Most *Chama* species form wholly aragonitic shells [39,40], however, some species form an outer shell layer that consists of rows of pointy calcitic ornamentations [41,42]. The valves of juveniles are symmetrical to one another, in contrast to the shells of adult animals [41,43]. The loss of symmetry of the two valves with increasing age is due to an enlarged umbonal region in the left valve and is called forth by the attachment [41,43]. Adult *Chama* individuals have large, particularly elongated adductor muscles [40]. These induce and regulate rapid and prolonged closure of the valves and are, obviously, necessary, as the ligament of Chamidae is very weak [43–45].

By using electron backscatter diffraction (EBSD), field emission scanning electron microscopy (FE-SEM), laser confocal imaging and depth-sensing nanoindentation, we characterise shell and myostracum microstructure, texture, hardness and indentation elastic modulus of *Chama* and *Glycymeris* shells. We place particular interest in understanding the structural and material property characteristics of myostraca and the changeover from the non-myostracal, valve, to myostracal microstructures and textures. We investigated the structural characteristics of two myostraca, the adductor myostracum and the pallial myostracum. We discuss first (i) whether the difference in habitat and lifestyle causes significant differences in non-myostracal valve and myostracum microstructure, texture and material properties. Subsequently (ii), we investigate whether valve activity, coordinated by muscle contraction and release, initiates differences in microstructure and texture of the myostracum at adductor muscle attachment sites. Different bivalve lifestyles, such as cementation to substrate, reclining on substrate surface, burrowing into muddy sediment or active

swimming rely on differences in valve movement speed as well as strength and duration of valve closure and opening. At last, (iii) we discuss whether variation in valve action affects myostracal hard tissue microstructure, texture and material properties.

2. Materials and methods

2.1. Materials

We investigated two *Chama* and three *Glycymeris* species, *Chama arcana, Chama gryphoides* and *Glycymeris bimaculata, Glycymeris nummaria* and *Glycymeris pilosa*, respectively. Care was taken that all investigated specimens were shells of adult organisms. Specimens of *G. bimaculata* were provided by the Bavarian State Collection of Zoology (ZSM) and *G. pilosa* was sampled in the Pasman channel, Adriatic Sea. Specimens of *G. nummaria* were collected from infralittoral environments close to Benalmádena (Málaga, Spain). *C. arcana* was sampled near Newport Beach, CA, USA, and obtained from collections of the Natural History Museum (London, UK).

2.2. Methods

2.2.1. Sample preparation for electron backscattered diffraction (EBSD) measurements and nanoindentation testing

Figs. AP1 to AP5 indicate the cuts through the shell and the sites where EBSD maps were taken. For all investigated species, the cut through the shell crossed the adductor myostracum, often, the pallial myostracum and the surrounding shell layers. *G. bimaculata, G. nummaria* and *G. pilosa* shells were cut in oblique and transverse directions. The shell of *C. arcana* was cut perpendicular to the hinge. The shell of *C. gryphoides* was cut transversely through the sites of both, anterior and posterior adductor muscles. The obtained shell pieces were embedded into epoxy resin and were subjected to several mechanical grinding and polishing steps. The final polishing step consisted of etch-polishing with colloidal alumina (particle size ~ 0.06 μm) in a vibratory polisher. Samples were coated with 4–6 nm of carbon for EBSD analysis, with 5 nm Pt/Pd for SEM imaging. For laser confocal imaging and nanoindentation testing, sample surfaces were not coated.

2.2.2. Secondary electron (SE), backscatter electron (BSE) imaging and electron backscattered diffraction (EBSD) measurements

SE, BSE imaging and EBSD measurements were carried out with a Hitachi SU5000 field emission SEM, equipped with an Oxford Instruments NordlyNano EBSD detector and an X-Max 80 × 80 EDS detector. EBSD scans were taken at 20 kV and were performed with a step size of 200 to 450 nm. For indexing the aragonite EBSD patterns the unit cell setting: $a_0 = 4.9614(3)$ Å, $b_0 = 7.9671(4)$ Å, $c_0 = 5.7404(4)$ Å was used. EBSD data were evaluated with the Oxford Instruments AZTEC and CHANNEL 5 HKL software and are presented as colour-coded crystal orientation maps, corresponding band contrast measurement maps and corresponding pole figures presenting individual orientation data points or their density distributions.

For a comprehensive understanding of non-myostracal shell and myostracum microstructure, samples were scanned with many EBSD measurements. On *G. nummaria* and *G. bimaculata* shells, we measured, for each species, 15 EBSD maps. *G. pilosa* shells were mapped with 5 measurements, on *C. arcana* and *C. gryphoides* shells we conducted, for each species, more than 20 measurements.

2.2.3. Nanoindentation testing

Nanoindentation measurements were conducted on *G. bimaculata* and *G. nummaria* using an MTS Nano Indenter XP (Nano instruments, USA), and on *C. arcana,* geological aragonite and geological calcite using a Nanoindenter G200X (KLA, USA) at Institute for Energy- and Climate Research (IEK-2), Forschungszentrum Jülich GmbH, Jülich, Germany, equipped with a standard diamond Berkovich tip (indentation elastic

modulus 1141 GPa, Poisson's ratio 0.07). Before each set of experiments, the tip area function and the frame stiffness were calibrated using a standard reference material, i.e., fused silica (indentation elastic modulus 72.12 GPa, Poisson's ratio 0.179). The quasi-static method was used at a constant indentation strain rate of 0.05 s^{-1}, and the peak holding time was 10 s for each test at a maximum depth of ~300 nm (XP) or a maximum load of ~9 mN (G200X) corresponding to a maximum depth of around 300 nm as well. The drift was determined at 90 % of the unloading segment (10% of the maximum load) during unloading for a drift correction. The indentation elastic modulus and the hardness values were determined via the unloading curve according to the Oliver-Pharr method [46,47]. The *C. gryphoides* samples were tested using a Triboindenter TI-950 nanomechanical tester, Hysitron, USA at the Department of Biomaterials, Max-Planck Institute of Colloids and Interfaces, Potsdam, Germany. A load function of 5s-2s-5s (loading-holding-unloading) with a peak force of 12mN and a holding time of 2 s at maximum load was applied at each measurement.

2.2.4. Terminology

Subsequently, we define structural and material property terms that we use in this study. For further information concerning EBSD see [48]. Information related to twin formation, see [49–51].

Microstructure refers to the sizes, morphologies, co- and mis-orientations, and modes of interlinkage of grains in a material. It is shown with coloured EBSD maps, where similar colours reflect similar crystal orientations and different colours highlight differences in crystal orientation. The acquisition coordinate system is indicated in the a-axes pole figures in Fig. 1a, b and is consistent for all EBSD scans presented in this contribution.

Pole figures are stereographic projections of crystallographic axes orientations measured for all pixels of an EBSD map or selected areas (subsets). The viewing direction of the pole figures is the same as the viewing direction of the corresponding EBSD maps. All pole figures shown here display the lower hemisphere. Showing data points on the lower hemisphere of the stereographic projection ensures that the pole
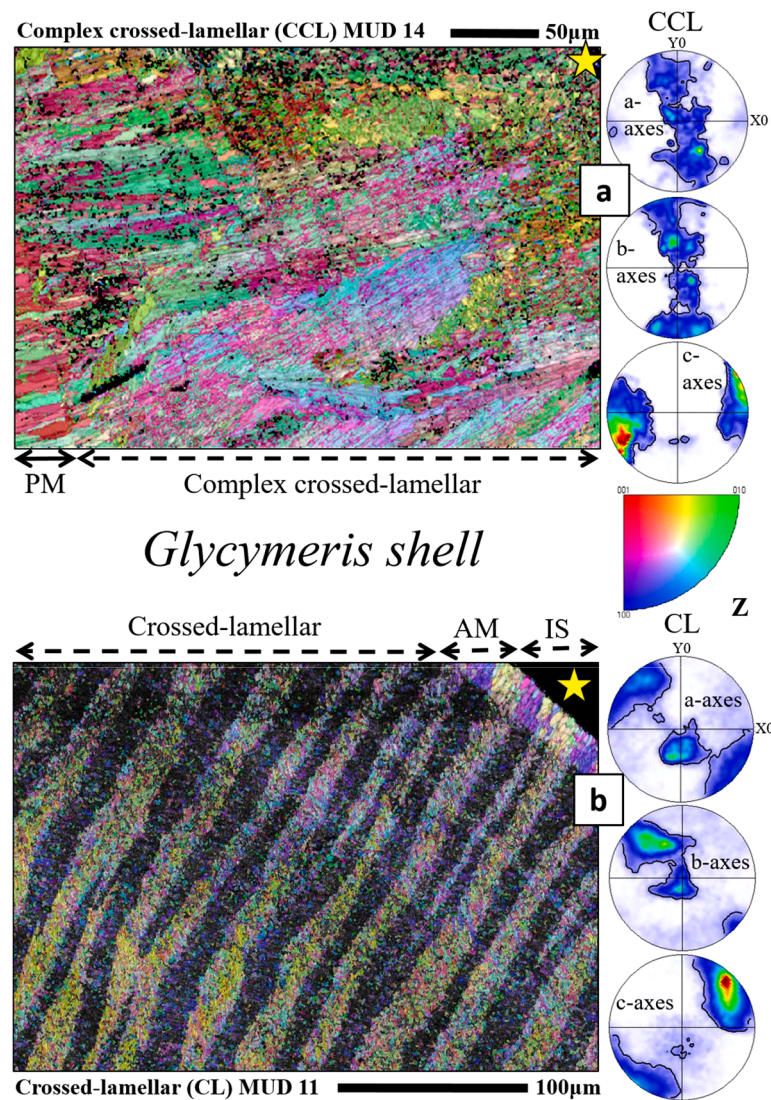

Fig. 1. EBSD scans depicting the different microstructures of non-myostracal *Glycymeris* shells. (a): a transversely (a) and (b) an obliquely sectioned shell of *G. bimaculata*. IS: inner shell surface, AM: adductor myostracum, PM: pallial myostracum, yellow star in (a) and (b): inner shell surface. From the outer towards the inner shell surface, *Glycymeris* shells comprise a crossed-lamellar (CL), the myostracal and the complex crossed-lamellar shell layer (CCL). The complex crossed-lamellar layer (a) consists of differently oriented clusters/blocks of small prisms and fibres. The crossed-lamellar layer (b) consists of arrays of first-order lamella, with each first-order lamella formed of two sets(b); the sets are inclined to each other. In *Glycymeris* the first-order lamellae run perpendicular to inner shell surface (b). The pole figures indicate the acquisition coordinate systems and show the orientational probability density distribution for the complex crossed-lamellar (a) and the crossed-lamellar sections (b), respectively. We observe a 3D "single-crystal-like" texture. However, in comparison to the complex crossed-lamellar valve portion, the 3D "single-crystal-like" texture is significantly better developed for the crossed-lamellar layer.

figures are displayed in the same spatial orientation as the corresponding EBSD map. With pole figures we either show individual orientation data points or the density distributions of the orientation data.

Texture or *crystallographic preferred orientation* relates to the distribution of all crystal orientations within a material. It is illustrated with pole figures which show either the colour-coded orientation data or the contoured version of the density distribution of the a-, b-, and c-axes poles. We observe in our study two texture modes: (i) a three-dimensionally ordered, 3D "single-crystal-like" texture and (ii) an axial/cylindrical texture.

A *3D "single-crystal-like" texture* is present when clear-cut maxima are observed in the pole figures of all crystallographic axes. Accordingly, for calcite, we need to observe in the pole figure one cluster for the c-axes and three clusters for the a*-axes; for aragonite one maximum in the pole figure for the a, - b- and c-axes, respectively.

An *axial/cylindrical texture* is developed in the relevant material when the c-axes show a cluster in one particular direction and the a- and b-axes scatter in orientation on a great circle, perpendicular to the c-axis orientation.

Crystal co-orientation statistics are derived from Kikuchi patterns measured at each pixel of an EBSD map. The degree of aragonite/calcite co-orientation within individual crystals is obtained from measurements of the orientational density distribution, the MUD value.

The *MUD* (multiple of uniform (random) distribution) value is calculated by the CHANNEL 5 EBSD software and is an indication of the strength of crystal co-orientation. A high MUD indicates high crystal co-orientation and low MUD values indicate low to random crystallite and/ or mineral unit co-orientation. The parameters for data contouring in the pole figures were fixed to a half width of 5 and a cluster size of 3, to maintain comparability for all measurements shown in this contribution. For a half width of 5 and a cluster size of 3 an MUD value of 700 indicates single-crystallinity, an MUD value of 1 indicates poly-crystallinity. The given MUD values indicate the crystal co-orientation strength for the described section or subset of an EBSD scan and does not apply to the entire volume of a microstructure.

The EBSD *band contrast map* depicts the signal strength of the Kikuchi pattern at each measurement point in the EBSD scan. It is displayed as a grey-scale component in the map; white to light grey colours indicate a high intensity of the Kikuchi signal, corresponding to strong mineralization, dark grey and black colours point to a weak or absent Kikuchi signal, e.g. when organic matter, is scanned.

Twinned crystals are entities in which adjacent crystals of the same phase are intergrown in a regularly recurring orientation relationship. These crystal orientation states are addressed as the twin domains of a twinned crystal. A regular planar interface of two twin domains is called the composition plane and such a twin is called a contact twin. If the interface is not confined to a plane (or planes), the twin is called a penetration twin. Twinning can occur during the initial growth of the crystal, or, it might take place after its formation, resulting from stress or phase transformation. The orientation relationship for the characteristic twin in question is called the twin law.

If a twinned entity contains domains of two orientation states, alternating in succession, we call it a *polysynthetic twin*. In biological materials, such twins do not show perfectly planar and parallel composition planes, as would be required by the definition of Hahn and Klapper [49], who, however, focused only on inorganic materials.

If a twinned entity contains three intergrown domains that are related by a twin law consisting of mirror operations on (110) and (-1 1 0), then we call it a *cyclic twin*. If these three orientation states occur multiple times within an entity as striations or fine parallel lines, we term the twinned crystal a *polycyclic twin*.

In this contribution, we prove the presence of twinned aragonite with the, for the twin law, specific misorientation boundary. For aragonite, the misorientation at the twin boundary is around 64°. We show, for this misorientation angle, the characteristic peak in the misorientation angle distribution diagram. We prove also the presence of twinned aragonite

with crystal misorientations shown in the relevant pole figures.

The shell surface of many *Chama* species is covered with calcium carbonate *ornamentations*. These are developed as ribs and are thin spicule- to blade-shaped hard tissue protrusions that are often arranged on the surface of the shell in an ordered pattern [40,41].

3. Results

This study details the structural and material property characteristics of *Glycymeris* and *Chama* shells. We describe first the microstructure and texture of the valves (without the myostracal layers and patches) and that of the ornamentations (Figs. 1–3, appendix Figs. AP6–AP8). Subsequently, we describe structural characteristics of adductor and pallial myostraca (Figs. 4, 5, appendix Figs. AP9, AP10) and the changeover between valve and myostracal layers (Figs. 6–8, appendix Figs. AP11–AP13). At last, we present specific structural and physical properties of *Glycymeris* and *Chama* valve and myostracal hard tissues, such as the presence and distribution of twinned aragonite and discuss hardness and indentation elastic modulus properties of the valves and of the myostraca (Figs. 9–12, appendix Figs. AP14–AP19). For a comprehensive visualisation of the observed microstructures, each colour-coded crystal orientation map (Figs. 1–10) is complemented with the corresponding, grey-scaled, band contrast measurement map given in the appendix (Figs. AP6–AP13). Aragonite and calcite textures are shown with pole figures (Figs. 1–10 give the contoured version of orientation data, Figs. AP6–AP13 give orientation data points).

The shells of *Glycymeris bimaculata, Glycymeris nummaria* and *Glycymeris pilosa* consist entirely of aragonite. The shell of *Chama arcana* is formed of aragonite and calcite. The ornamentations of *C. arcana* are calcitic, the layers of the shell are aragonitic. The shell and ornamentation of *Chama gryphoides* are solely aragonitic.

Irrespective of the myostraca (adductor, pallial), the valves of the investigated *Glycymeris* species comprise *two layers*. The investigated *Chama* species construct their valves with *three layers*, including the ornamentation layer. Myostraca are considered to be additional layers to those of the non-myostracal valves. For all investigated species, the mode of crystal arrangement varies significantly for the different shell layers.

Figs. 1 and AP6 visualise *Glycymeris* shell microstructure in the complex crossed-lamellar (inner shell layer) and the crossed-lamellar layer (outer shell layer), respectively. The complex crossed-lamellar layer (Fig. 1a) exhibits an intricate crystal orientation pattern consisting of numerous, differently oriented, clusters/entities/blocks formed of small, rather granular to prismatic crystals. As the colour-coded EBSD map (Fig. 1a) shows, these crystal entities/blocks vary considerably, to some degree randomly, in orientation. The crossed-lamellar layer (Fig. 1b) consists of assemblies of small, lath-shaped, crystals organised into first-order lamellae. A first-order lamella comprises a set of crystallographic orientations. Crystals within the set1 lamella have an opposing inclination to the crystals of the set2 lamella (e.g. [25,26]). In *Glycymeris* shells, the first-order lamellae run almost perpendicular to the inner shell surface and growth lines (Figs. 1b, AP6b). This is not the case for the investigated *Chama* shells (Fig. 2a).

Chama shells are formed of three shell layers (Figs. 2, 3, AP7, AP8). For *C. arcana* we observed complex crossed-lamellar aragonite at inner and crossed-lamellar aragonite at outer shell portions (Figs. 2, AP7). The outermost layer is calcitic and its surface is covered by rows of calcitic ornamentations (Figs. 3, AP8). The crossed-lamellar microstructure of *Chama* (Figs. 2a, AP7a) comes close to the crossed-lamellar crystal arrangement of *Glycymeris* shells. In *Chama* as well, crossed-lamellar aragonite is formed of first-order lamellae that comprise two sets of lamella that are arranged at an angle to each other. The two sets of first-order lamellae consist of minute, lath-shaped crystals. Carter [52] described different types of crossed-lamellar arrangements and suggested that interlacing of first-order lamellae is always given in crossed-lamellar microstructures. When we compared the degree of
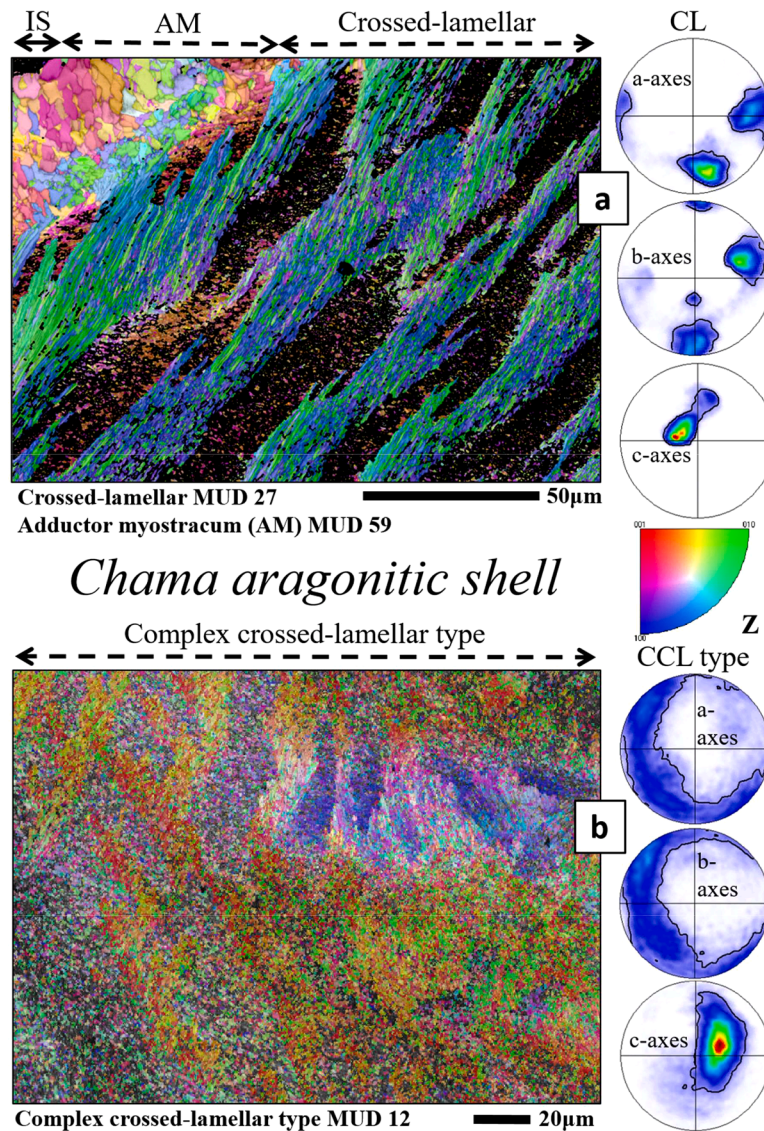
Fig. 2. EBSD scans depicting the microstructures of non-myostracal *Chama* shells. IS: inner shell layer, AM: adductor myostracum, CL: crossed-lamellar, CCL type: complex crossed-lamellar type. The valves of *C. gryphoides* comprise a crossed-lamellar layer and an adductor myostracum along the inner surface of the shell. A complex crossed-lamellar type microstructure forms the outer shell layer and shell ornamentation. The latter microstructure consists of small crystals arranged with an intricate orientation pattern (b). Pole figures show the orientational probability density distribution for the crossed-lamellar (a) and the complex crossed-lamellar type layers (b) and highlight, for the crossed-lamellar shell, a 3D "single-crystal-like" (a) and for the complex crossed-lamellar shell an axial (fibre) (b) texture, respectively.

interlacing between the crossed-lamellar shell of *Glycymeris* and that of *Chama*, we found that, in contrast to *Glycymeris*, in *Chama* shells adjacent lamellae are rarely parallel to each other and more strongly interlaced (compare Figs. 1b and 2a). To our opinion, this is not due to a cut effect as, to trace the topological relation of the two sets of a first-order lamella, we sectioned *Chama* shells in different directions and scanned them with EBSD.

The shell of *C. gryphoides* is entirely aragonitic. We found a layer of complex crossed-lamellar aragonite at the innermost shell sections. Adjacent to the latter, towards the outer shell surface, crossed-lamellar aragonite is developed for this *Chama* species as well with, as it is the case for *C. arcana* shells, the set1 and the set2 lamellae being rather interlaced. The outermost shell layer and ornamentation of *C. gryphoides* shells is formed of granular aragonite (e.g. Fig. 2b) that, only in some instances, comprises differently oriented aragonite clusters/entities. Hence, the microstructure of the outermost shell and ornamentation of *C. gryphoides* resembles, only to some extent, the complex crossed-lamellar arrangement pattern of crystals in the investigated *Glycymeris*

and *C. arcana* shells. (Figs. 2b, AP7b). We addressed the latter microstructure as a complex crossed-lamellar type structure that occurs at outer shell layers. According to Taylor et al. [23] and Kennedy et al. [40], the complex crossed-lamellar microstructure for *Chama* and *Glycymeris* is only present at inner valve sections.

For *Glycymeris* and the aragonitic microstructures of the investigated *Chama* species, we found a smooth transition from the crystal orientation pattern of one shell layer into the other. Hence, there is a continuity of aragonite crystal crystallographic axes from one aragonitic microstructure to the other (e.g., Figs. 1a, b, 2a). However, we did not observe a smooth transition between calcitic ornamentations and the aragonitic shell in *C. arcana* (Figs. AP4c, AP5a, b). In the latter, the calcite of the ornamentation is separated from the aragonitic layers by a thick, layered, organic deposit (grey sheet in Fig. AP5b).

The microstructure of the ornamentation ribs of *C. arcana* is very specific and different to the microstructures of the other shell layers (Figs. 3, AP8). We observed a gradual increase in crystal size away from the outer surface of the ornamentation ribs. Hence, the largest crystals of
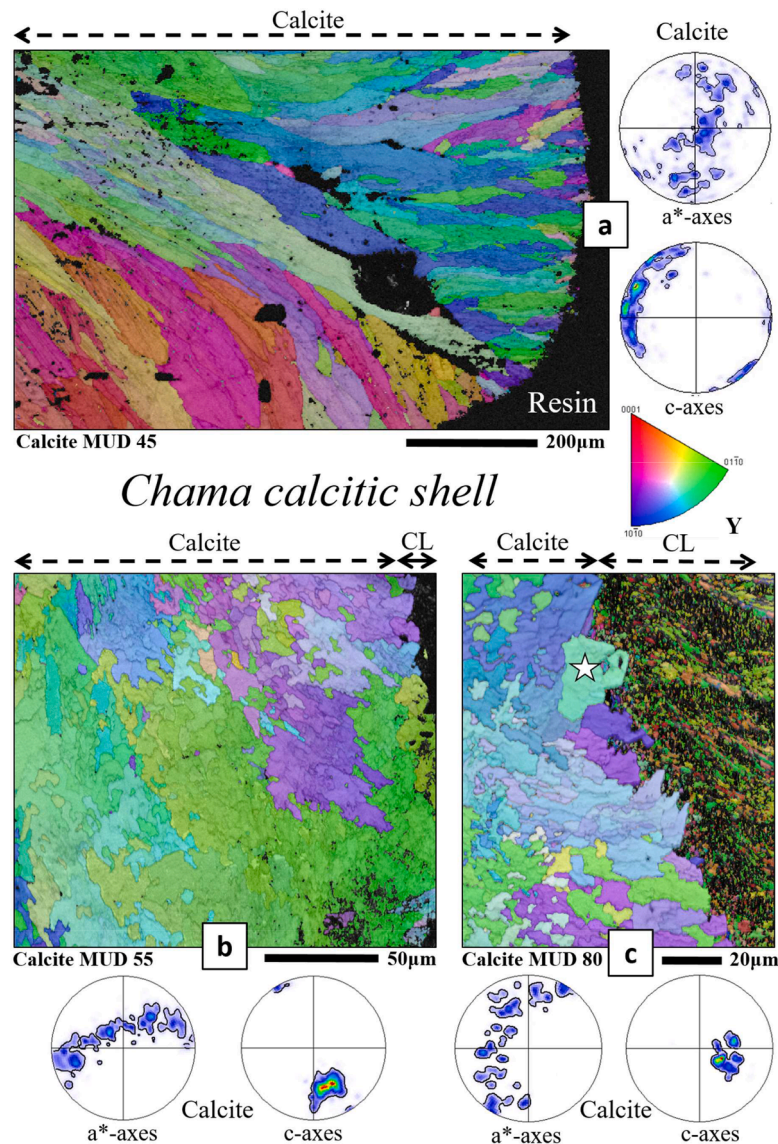
Fig. 3. EBSD scans depicting the microstructure of the calcitic ornamentation of *Chama shells.* The calcitic ornamentations of *C. arcana* comprise large crystal clusters with the calcite c-axis being perpendicular to the ornamentation surface (a). Within the ornamentation, the calcitic crystals interconnect in a complex mode in 3D (b, c). Towards the inner shell, the calcite crystals are interconnected in a complex way with the aragonitic crossed-lamellar layer (CL). The calcite crystals have rhombohedral, idiomorphic, crystal morphologies (b, c). Pole figures show the orientational probability density distribution for the crystals shown in the corresponding EBSD maps and illustrate that ornamentation calcite has an axial (fibre) texture.

the ornamentation ribs are adjacent to the crossed-lamellar shell layer. We find that calcite c-axes are perpendicular to the outer surface of the ornamentation; they rotate with the curvature of its outer shell surface (Figs. 3a, AP8a). Most interesting is the habitus of crystals that form the ornamentation ribs as well as the nature of their interlinkage (Figs. 3b, c, AP8b, c). The crystals or crystal units have highly fractal morphologies and interlock strongly in 3D (Figs. 3b, c, AP8b, c). In addition, we observed calcite crystals with idiomorphic morphologies in the biologically secreted ornamentation (white star in Fig. 3c, black star in Fig. AP8c and [53]). The structural characteristics that we found for *Chama* ornamentation ribs are rarely observed for biologically secreted hard tissues and convey some information on the formation process of the ornamentation calcite. Biocarbonate crystals with dendritic-fractal morphologies and the crystals interdigitating strongly in 3D have so far been observed for brachiopod primary shell layer calcite [54] and rotaliid foraminifera shell calcite [55].

Figs. 4–8 and appendix Figs. AP9–AP13 visualize the microstructure and texture of adductor and pallial myostraca as well as topological

characteristics at the changeover of the non-myostracal, valve, structures (crossed-lamellar, complex crossed-lamellar microstructure) to that of the myostraca. In comparison to the non-myostracal layers of the valves, the myostracal layers comprise less organic substance [25,26]. For all investigated species, adductor myostraca are always adjacent to the crossed-lamellar portion of the shell (Figs. 6–8a, AP11–AP13a), while the pallial myostracum is always between the crossed-lamellar and the complex crossed-lamellar layers of the valves (Figs. 7, 8, AP12b, AP13b). At the crossed-lamellar - myostracum interface (Figs. 4a–6), myostracal aragonite consists of minute/small, granular-prismatic, crystals (Average grain size around 10 μm). These increase in size towards the inner shell surface (Average grain size larger than 100 μm). Pole figures (e.g. Figs. 4, 6) illustrate that the aragonite c-axes orientation is normal to the inner shell surface. These structural characteristics evidence that *Glycymeris* and *Chama* myostracal aragonite has a 'competitive growth type' microstructure. Crystal formation through growth competition implies that at nucleation many crystals form close to each other (Figs. 4a, AP11) and, at growth, compete for
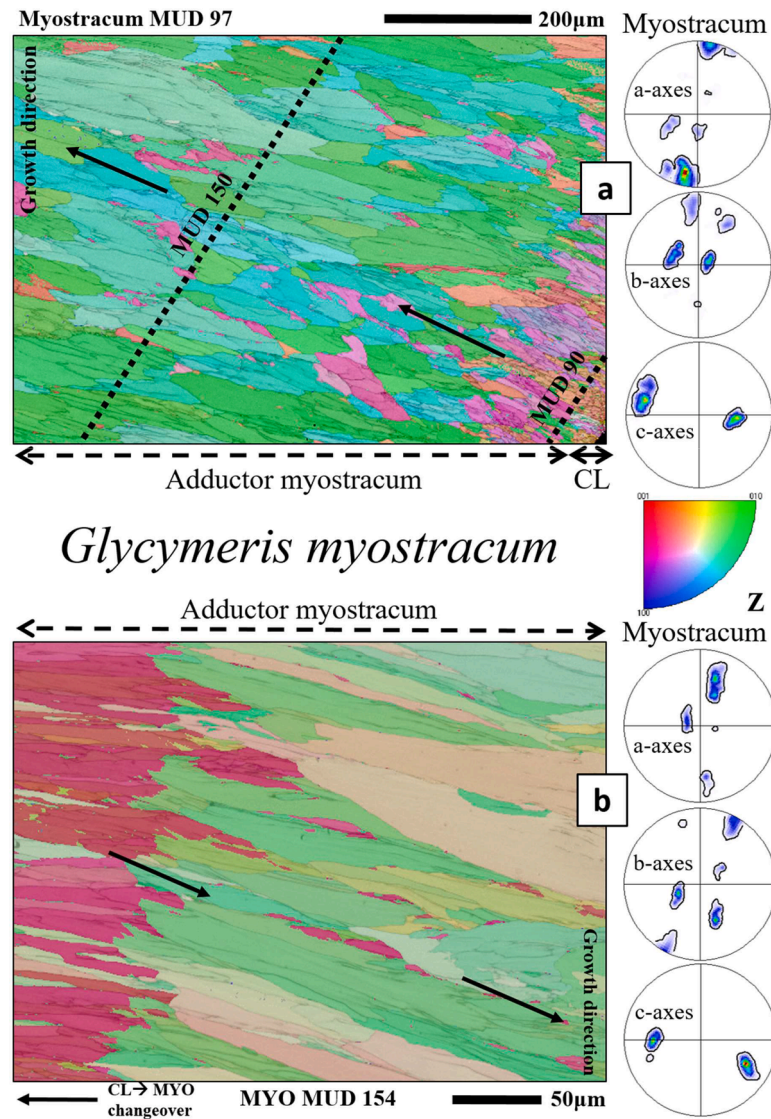
Fig. 4. EBSD scans visualizing the microstructure of the adductor myostracum in *Glycymeris* shells. Visible in (a) is the competitively grown microstructure of *G. bimaculata* adductor myostracum and the interface between myostracal to the crossed-lamellar valve layer (CL). Myostracal (MYO) crystals close to the crossed-lamellar shell are minute to small (average grain size 25 μm) and isotropic in shape (a). As implied by the MUD values of different subsets, the crystal co-orientation increases towards the inner shell surface. (a). The crystals become larger and assume prismatic shapes towards the growth direction indicated by black arrows (a, b). The second EBSD map depicts the microstructure of the adductor myostracum in *G. nummaria* (b). It features an assembly of large myostracal prisms and a sharp boundary in crystal orientation (b). Pole figures depict the orientational probability density distribution for the respective myostracal layers and show a 3D "single-crystal-like" texture.

space. The likelihood for a small crystal to grow to a large entity is inversely proportional to the deviation of the crystal growth direction from an orientation normal to the nucleation template. The result of the growth competition process is a strong decrease in the number of crystals, as one moves away from the nucleation substrate, accompanied by an increase in crystal size and generation of a progressively stronger crystallographic preferred orientation (Fig. AP11). Thus, at inner shell surface, aragonite c-axes are almost parallel to each other. This structural characteristic is observed in all investigated *Glycymeris* and *Chama* species, for pallial as well as adductor myostraca. For *Glycymeris* and *Chama*, Figs. 7, 8, AP12 and AP13 show the changeover from crossed-lamellar to the adductor myostracal layer as well as from pallial myostracal to the complex crossed-lamellar part of the shell. We find assemblies of small/minute crystals always at the transition from crossed-lamellar to the myostracal structure and not at the transition from myostracal to complex crossed-lamellar microstructure. Figs. 4, AP9 and Figs. 5, AP10 highlight, for the investigated *Glycymeris* and

Chama species, a significant difference in the morphology of adductor myostracum prisms. This marked difference between *Glycymeris* and *Chama* in myostracal crystal shape is not caused by a cut effect; we checked this with EBSD measurements, carried out on different cuts through the valves and myostraca. We find also that the crystallographic texture, visible from the pole figures, varies between the two genera. *Glycymeris* usually shows a 3D "single-crystal-like" texture (with orientational density maxima and high crystal co-orientation, Figs. 4, AP9)), whereas the texture in *Chama* myostraca is mostly axial (fibre texture) with the a- and b-axes orientations varying evenly on a great circle (Figs. 5, AP10).

For *Glycymeris* and *Chama*, Figs. 6–8a highlight the changeover from crossed-lamellar to myostracal layers. It is well observable that crystal orientation is transmitted from one layer to the next (see the white arrows indicating a continuation in colour from one microstructure to the other in Figs. 6a, 7a), even though for the two adjacent layers, crystal morphologies, sizes and growth modes are different. Furthermore, as
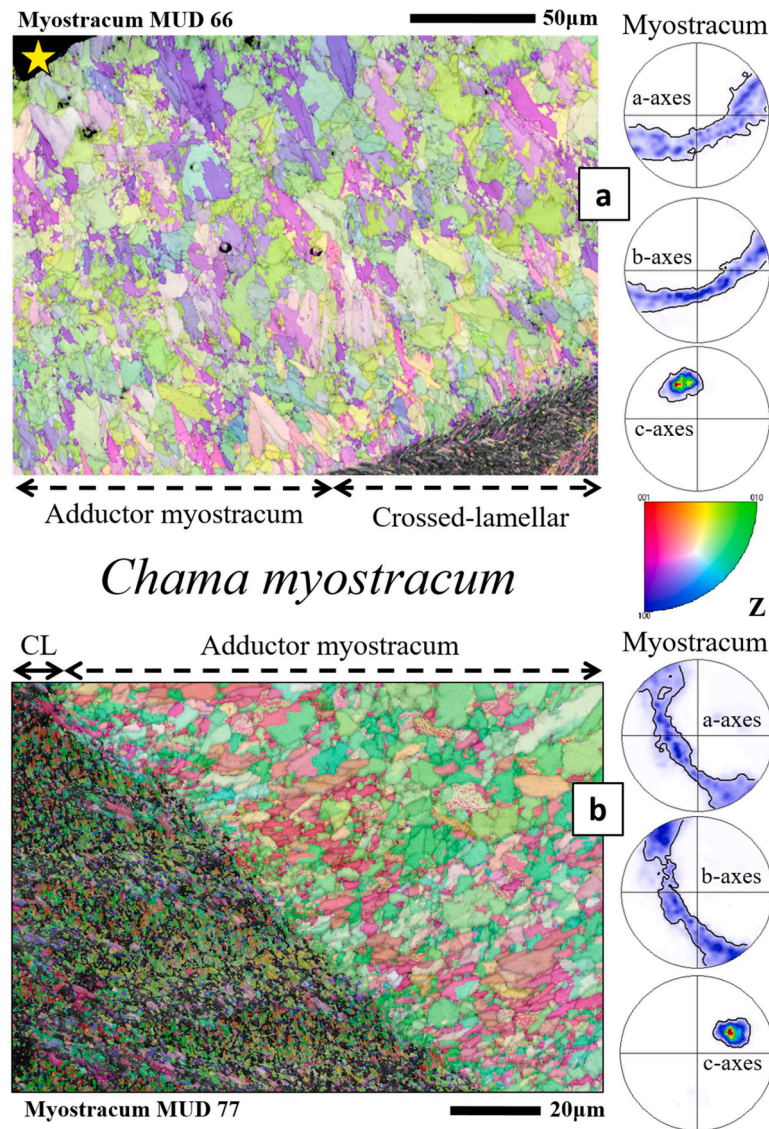
Fig. 5. EBSD scans depicting the microstructure of the adductor myostracum of *Chama* shells. In (a) we show the competitively grown adductor myostracum of *C. gryphoides*, from the interface with the crossed-lamellar shell (CL) up to the inner shell surface (yellow star in (a)). In (b) we highlight the adductor myostracum microstructure of *C. arcana*, also starting from the interface with the crossed-lamellar shell. The microstructure of *Chama* adductor myostracum is intricate. Crystal morphologies are very irregular in shape, size and organisation and show only vaguely prismatic morphologies. The competitive growth microstructure is not as obvious as it is the case for *Glycymeris* shells (e.g. Fig. 4a). Pole figures visualize the orientational probability density distribution for myostracal shell portions and highlight for *Chama* adductor myostraca an axial (fibre) texture.

Figs. 6a and 7a demonstrate, one can observe the continuation of the first-order lamellar microstructure into the myostracal part of the shell. The crossed-lamellar orientation pattern of crystals is transmitted to the adjacent myostracum and is continued, even with the competitive growth mechanism. In the texture of the myostracum, it is visible that the inherited orientations of the first-order lamellae coincide along one common a-axis (pole figures in Figs. 6b, AP11a). This characteristic is common for the crossed-lamellar orientation pattern and is discussed in more detail in [20,56,57]. The interface between the crossed-lamellar layer and the myostracum is not always straight. It can be serrated, with the two latter layers interlocking into one another (Fig. 7a). Towards the inner shell surface, the transition from the myostracum into the complex crossed-lamellar layer is remarkable (Fig. 7b). The large prismsforming during the most advanced stage of myostracal growth continue vestigially into the first-formed sections of the complex crossed-lamellar shell (yellow star in Fig. 7b). These crystals are partially traversed by polycyclic twins (the red pixels indicate the twinning, see the crystal marked with a yellow star in Fig. 7b) and merge

with the microstructure and mode of crystal orientation (texture) of the complex crossed-lamellar structure (Figs. 7b, 8b).

EBSD measurements allow the determination of misorientation between crystals. Figs. 9a, 10a, and AP19a show EBSD maps conducted on *G. nummaria, C. arcana* and *G. bimaculata*, respectively. The map in Fig. 9a covers the crossed-lamellar, pallial myostracal and complex crossed-lamellar microstructure, the map in Fig. 10a shows the prisms of the adductor myostracum. The map in Fig. AP19a depicts the pallial myostracum and the adjacent complex crossed-lamellar valve layer. With white lines, we highlighted the sites where we found a systematic misorientation of ~64° between adjacent crystals. At these sites, specific high-angle boundaries are present between adjacent crystals and connect these with a specific orientation relationship. These high-angle boundaries are twin boundaries; crystals connected by twin boundaries are the domains of a twinned crystal. The twin law of aragonite is a mirror reflection on the {110} plane, which is also the composition plane [49]. For aragonite, we find cyclic, polycyclic and polysynthetic twinning. Accordingly, with the white lines in Figs. 9a, 10a, AP14a we
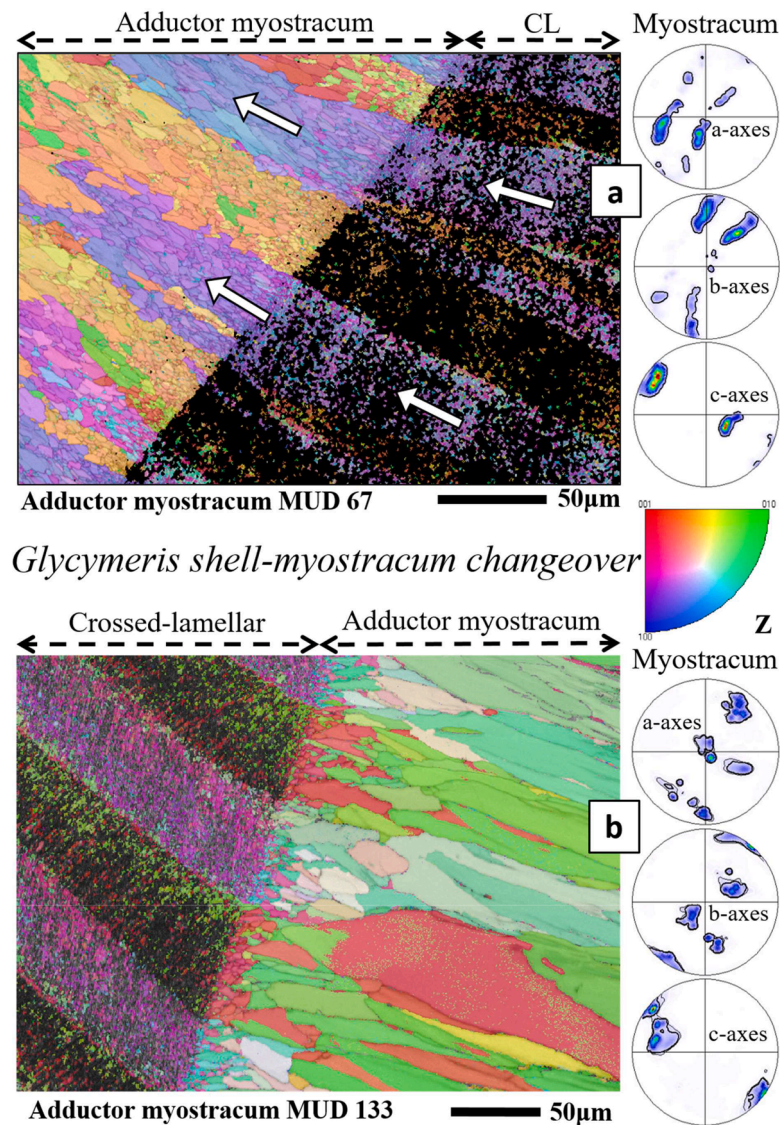
Fig. 6. EBSD scans visualizing for *Glycymeris* the changeover from crossed-lamellar to adductor myostracal microstructures. (a): *G. bimaculata*, (b): *G. pilosa*. It is well visible in (a) and (b) that the crystal orientation of the two sets of first-order lamellae of the crossed-lamellar (CL) microstructure is transmitted to the adductor myostracum (e.g., white arrows in (a)). Myostracal crystals close to the interface are granular and minute to small in size ((a), (b)), increase in size and become more prismatic towards the inner shell surface. The evolution of the crystal co-orientation towards the inner shell surface is depicted in appendix Fig. AP11. Pole figures show orientational probability density distribution for the myostraca and depict that these have a 3D "single-crystal-like" texture.

document the distribution and abundance of twinned crystals within the different shell layers. For the different layers, we observed differences in the degree of twinning (Figs. 9b, c, 10b, c, AP14a, b). In *Glycymeris* valves, the complex crossed-lamellar structure appears to be most twinned and the crossed-lamellar microstructure least twinned, respectively (Figs. 9a, b, AP14a, AP14b see the relative frequency – misorientation angle diagrams). However, it has to be noted that the relative misorientation frequencies may be affected by the amount of indexed data points for each layer. In the complex crossed-lamellar layer, twinning is mostly polycyclic and very abundant (Figs. 9a, AP14a). Within the myostracum, twinning is between the prismatic crystals and not within them (Figs. 9a, 10a, AP14a). For the crossed-lamellar layer, we observe polysynthetic twinning within each first-order lamella and cyclic twinning between adjacent set1 and set2 lamellae (Fig. 9a).

The texture of all valve layers, including the myostracal and ornamentation portions, is either 3D "single-crystal-like" (Figs. 1b, 2a, 4, 6, 7a, 8a) or cylindrical (Figs. 1a, 2b, 3, 5, 7b, 8b). For definitions of the texture modes see the *Terminology* part of the Methods section. The pole

figures demonstrate the similarity in c-axes orientation between the different valve layers, the different myostraca and the ornamentations (Figs. 1–8, AP6–AP14). Hence, crystal c-axis orientation is similar from the outermost ornamentation (calcitic or aragonitic), up to the innermost complex crossed-lamellar shell portion (aragonitic).

Figs. 11, 12, Table 1 and appendix Figs. AP14–AP19 show hardness and indentation elastic modulus results obtained from the different layers of *Glycymeris* and *Chama* shells, relative to the non-biological aragonite and calcite analogues. In *G. bimaculata* and *G. nummaria* (Fig. 11), the hardness of the myostracum surpasses the hardness of the (complex) crossed-lamellar shell layers and, significantly, that of the non-biological reference. When considering the indentation moduli of the investigated materials, it is well visible that, for both species, the myostracum and the (complex) crossed-lamellar layers are distinctly lower in indentation elastic modulus, relative to the non-biological aragonite reference. For both *Glycymeris* species, the range in indentation elastic modulus is similar for the valves and the myostracum (Fig. 11). For *C. gryphoides* and *C. arcana* myostracum, hardness is increased, relative to (complex) crossed-lamellar shell regions and
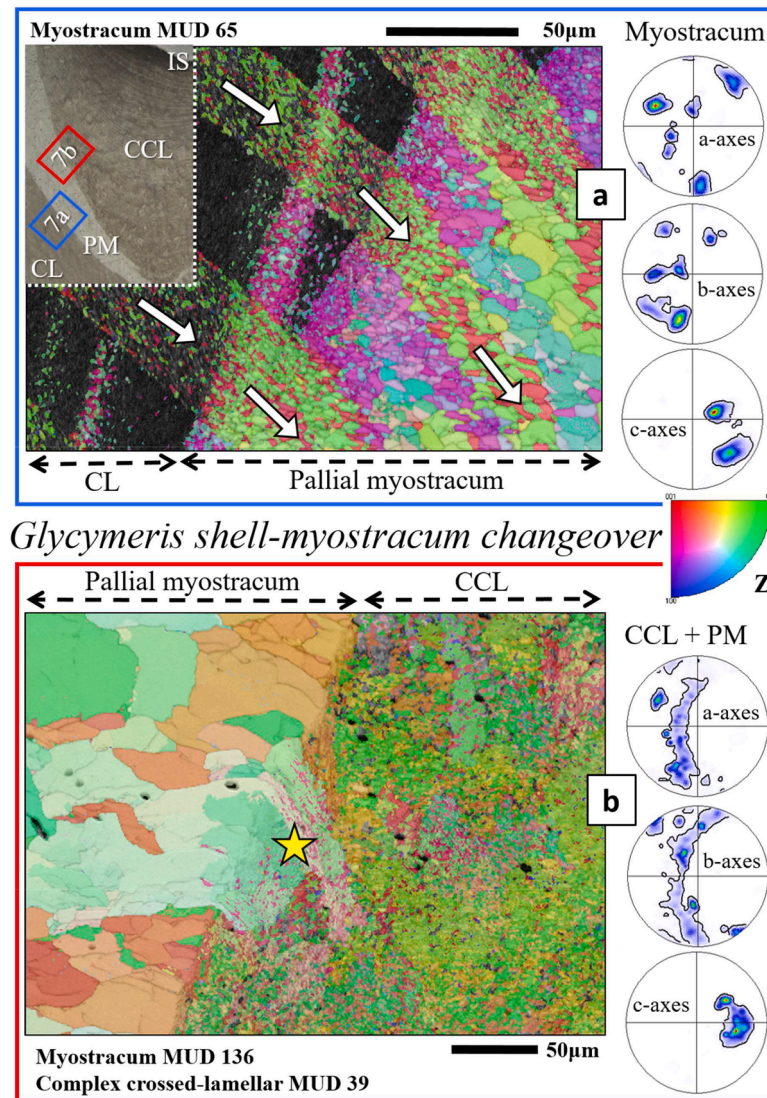
Fig. 7. EBSD scans visualizing for *Glycymeris* the changeover from crossed-lamellar to pallial myostracal (a) and from pallial myostracal to complex crossed-lamellar microstructures (b). For the position of EBSD scans see insert in (a). We visualize also the interface between crossed-lamellar – pallial myostracal and pallial myostracal – complex crossed-lamellar shell portions. The continuation in the orientation of the two sets of first-order lamellae into the myostracum (white arrows in (a)) is well observable. (b): the transition of the pallial myostracum (PM) into the complex crossed-lamellar layer (CCL) for a *G. nummaria* shell. Large myostracal prisms (yellow star in (b)) protrude into the complex-crossed lamellar layer. Along the sharp interface, they are interrupted by a boundary of polycyclic twinning on (110) and ($1\bar{1}0$) (around 64° misorientation) that commences in the complex crossed-lamellar layer. Pole figures indicate the orientational probability density distribution for the respective, non-myostracal, valve and myostracal layers and depict in (a) a single-crystal like texture and in (b) an axial (fibre) texture.

relative to the non-biological carbonate analogues. When compared to non-biological aragonite, (complex) crossed-lamellar shell layers and the myostracum are lower in indentation elastic modulus, than the reference. In contrast to *Glycymeris*, we observe for *Chama* a slight difference in indentation elastic modulus between (complex) crossed-lamellar layers and the myostracum. Hence, while for *Glycymeris* only the hardness is varied between the (complex) crossed-lamellar and myostracal valve regions, for *Chama,* we find for the myostracum and the rest of the valves a variation in hardness and a slight variation in indentation elastic modulus (Table 1).

4. Discussion

Bivalved molluscs live in a wide range of habitats and have developed a variety of lifestyles. While *Chama* is sessile and lives in turbulent waters at depths up to 30 m, *Glycymeris* populates calm waters, burrows superficially in the sediment and lives up to 200 m depth. Adjusting to different environments and leading different lifestyles demands adaptations of soft and hard tissue. For bivalves, adaptation include for example variations in shell size, form and thickness, modification of the foot, change in hinge ligament size and resilience, variation in muscle size, number and structure, and adjustments of organs [22,23,40,58,59]. In this study, we investigated structural and material property characteristics of the hard tissue of the non-myostracal and the myostracal parts of the valves for examples of mobile, infaunal, and sessile, epifaunal, bivalves. Of particular interest is to understand structural and physical property characteristics of those hard tissues where adductor and mantle muscles attach to the shell and to characterise the nature of the transition from non-myostracal, valve, to myostracal structures (Figs. 13–16, AP14–AP21). We complemented our discussion with EBSD results on the pedal myostracum of *Glycymeris glycymeris* [25,26], an EBSD measurement on the pallial myostracum of *Dosinia scalaris* (Fig. 15) and an EBSD measurement on the adductor myostracum of the bivalve *Placopecten magellanicus* (Fig. AP21).
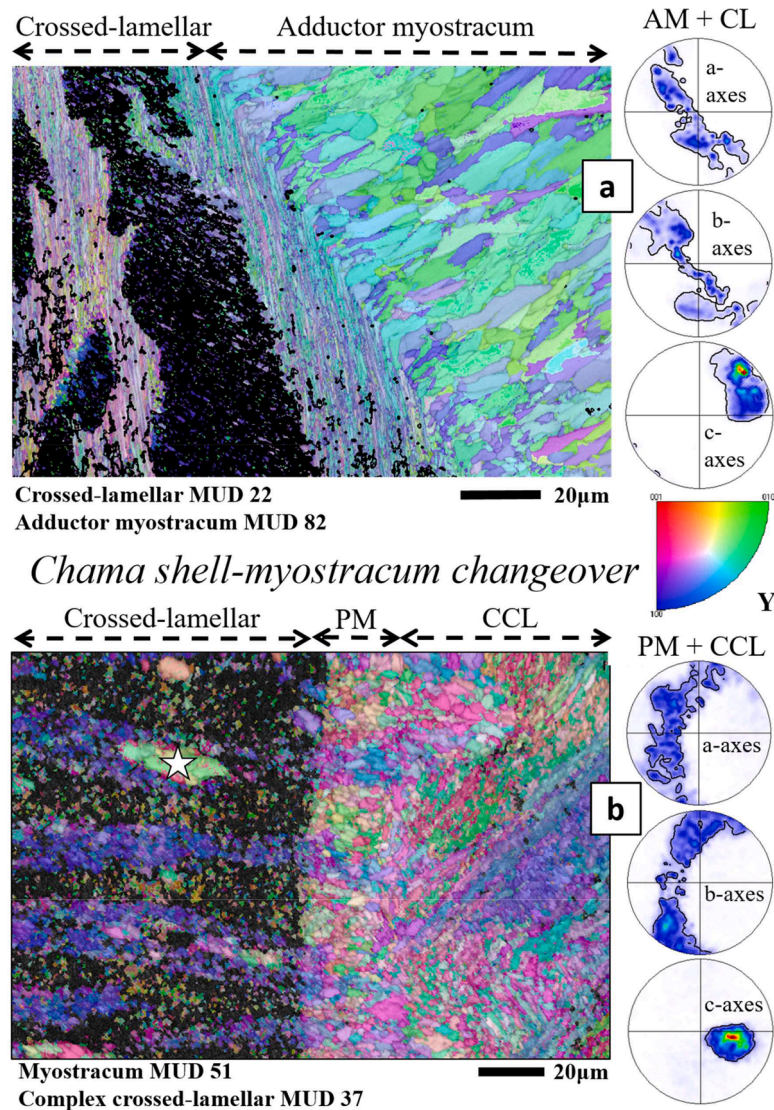
Fig. 8. EBSD scans depicting for *Chama* the changeover from the crossed-lamellar shell to the pallial myostracum (a). (b): the changeover from the crossed-lamellar shell to the pallial myostracum and from the pallial myostracum to the complex crossed-lamellar shell. (a): *C. gryphoides*, (b): *C. arcana*. CL: crossed-lamellar, CCL: complex crossed-lamellar, AM: adductor myostracum, PM: pallial myostracum. (a): Even though the sets of the crossed-lamellar structure run almost parallel to the interface between the two microstructures, the transmission of the crystal orientation pattern, from the crossed-lamellar to the myostracal shell, is still visible. (b): The crossed-lamellar layer comprises scattered, large single-crystal domains (white star in b) and its texture is transmitted through the pallial myostracum into the complex crossed-lamellar layer. Pole figures show the orientational probability density distribution for the non-myostracal, valve, and the two myostracal layers and depict an axial (fibre) texture.

Exerting control onto valve activity is essential for the survival of bivalves. The speed of valve movement, the time-dependent variation of valve opening and closure, and the strength of valve closure decide on the quality of soft tissue protection [60,61]. The opening/closing of the valves and the movement of the foot are determined by the action of adductor and pedal muscles [62–66]. For bivalves, the movements of muscles involve forces generated by antagonistic muscle contraction, muscle extension and relaxation [58]. Hence, depending on the motion in question, e.g., movement of valves and foot at burrowing or keeping the valves open or shut for longer periods, demands contraction and relaxation of the involved muscles, at diverse speeds and for diverse times [63–65,67]. To facilitate the latter requirements, a particularly strong, and, for the movement, appropriate attachment of the muscles to the valves has to be developed by bivalved organisms.

As described in the introduction, bivalve muscles attach to the hard tissue of the myostracum via a tendon cell layer. Myostracal scars and layers are always aragonitic and have an outstanding and characteristic microstructure that is distinct from that of the remaining shell, and have a specific hardness and indentation elastic modulus. The two sketches in Fig. 13 visualize on a larger scale for *Glycymeris* and *Chama* the interrelation between the observed, non-myostracal, valve and myostracal microstructures. We measured with a large series of EBSD scans (i) the transition from one myostracum into the other (from pallial to adductor and vice versa) and (ii) the myostracum in relation to the crossed-lamellar and the complex crossed-lamellar valve layers. In Fig. 13 we summarized our findings gained from EBSD scans and visualize structural characteristics and the topological relation of the different myostracal and non-myostracal valve crystal assemblies.

Subsequently, we discuss the following questions:

1. Are the microstructure, texture, and material properties of the non-myostracal parts of the valves, similar or different for the investigated *Glycymeris* and *Chama* species?
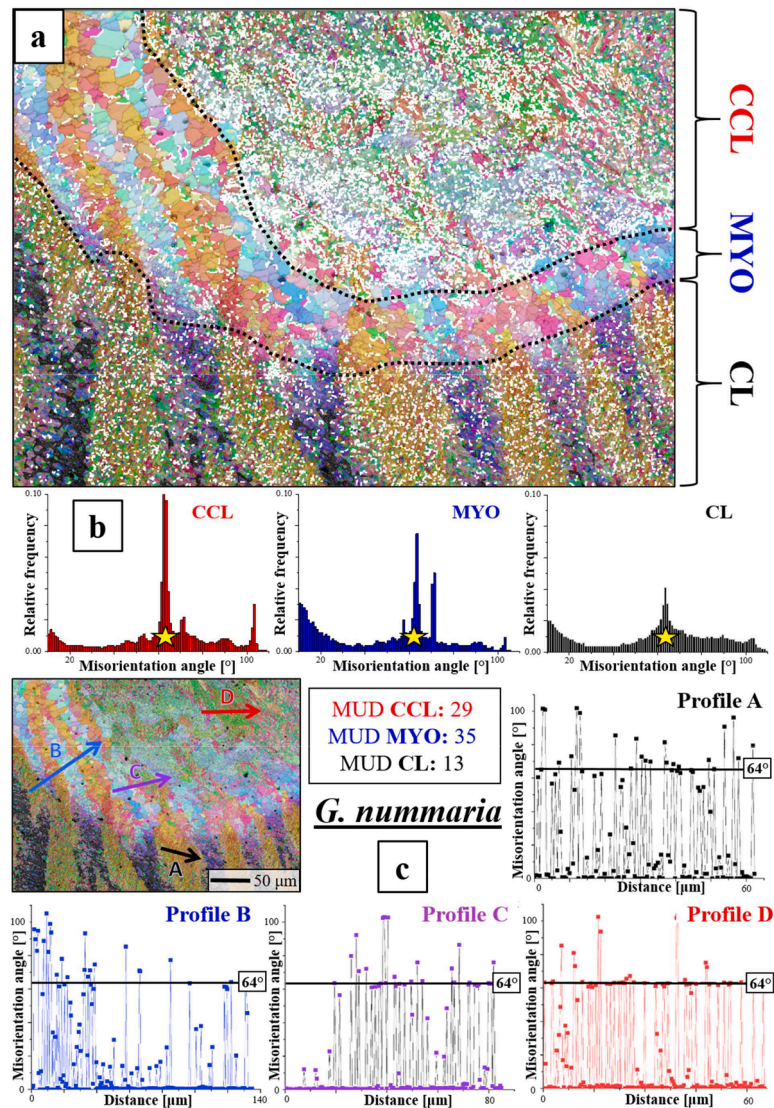
Fig. 9. Misorientation angle analysis of the different layers in an obliquely sectioned *G. nummaria* shell. The EBSD map (a) visualizes the three layers that are present in this measurement: Complex crossed-lamellar layer (CCL), myostracum (MYO) and crossed-lamellar layer (CL). Grain boundary angles between 63° and 65° are highlighted with white points in the EBSD map and indicate grain boundaries of twinned aragonite. The misorientation angle plots (b) show for all three layers peaks of varying relative frequency for a misorientation angle of 64° (indicated by yellow stars). Misorientation angle profiles (A-D) traversing the different layers provide further information about the type of aragonite twin (c).

2. Are myostracal microstructure, texture, and material properties similar or different for the investigated *Glycymeris* and *Chama* species? As described above, Glycymerididae and Chamidae do not share similar habitats and lifestyles.

3. What are the driving factors for structural similarity or difference?

The secreting cells?

The topological relation of muscle (adductor and pallial) and mantle cells to the hard tissue of the myostracum and to that of the non-myostracal valves?

Is a possible difference in the biomineralization process responsible for the difference in myostracum and valve structure?

4.1. The microstructure and texture of the non-myostracal layers

Kennedy et al. [39] and Taylor and Kennedy [68] reported for *Glycymeris* and non-calcitic *Chama* shells crossed- and complex crossed-lamellar aragonite crystal arrangement patterns. Our results confirm this; however, we observe for some *Chama* shells an additional

microstructure. We name the latter as a 'complex crossed-lamellar type' microstructure. For the investigated *Glycymeris* and *Chama* species, the non-myostracal (Figs. 1, 2) and myostracal (Figs. 4, 5) layers do show some comparable microstructural motifs, are, however, not entirely similar.

We observe for both, *Glycymeris* and *Chama*, the formation of first-order lamellae, arranged into two sets, with the latter having distinct crystal orientations. Each of the first-order lamellae comprises lath-shaped third-order lamellae. Despite the similarity in the internal structure of the first-order lamellae, we see, for *Glycymeris* and *Chama*, differences in set1 and set2 lamellae organisation and interlinkage (Figs. 1b, 2a, AP20). For *Glycymeris*, the first-order lamellae run strongly parallel to each other (Fig. AP20), while for *Chama*, they are less clear-cut in morphology and, in general, interlaced (Fig. AP20). In our opinion, this is most likely not caused by a cut effect, as this interlaced mode of first-order lamella set organisation for *Chama* shells was observed for shells sectioned along various orientations (see Methods section). A structural effect in lamella orientation, relative to the myostracum, is that in *Glycymeris* first-order lamellae are at an angle of, more
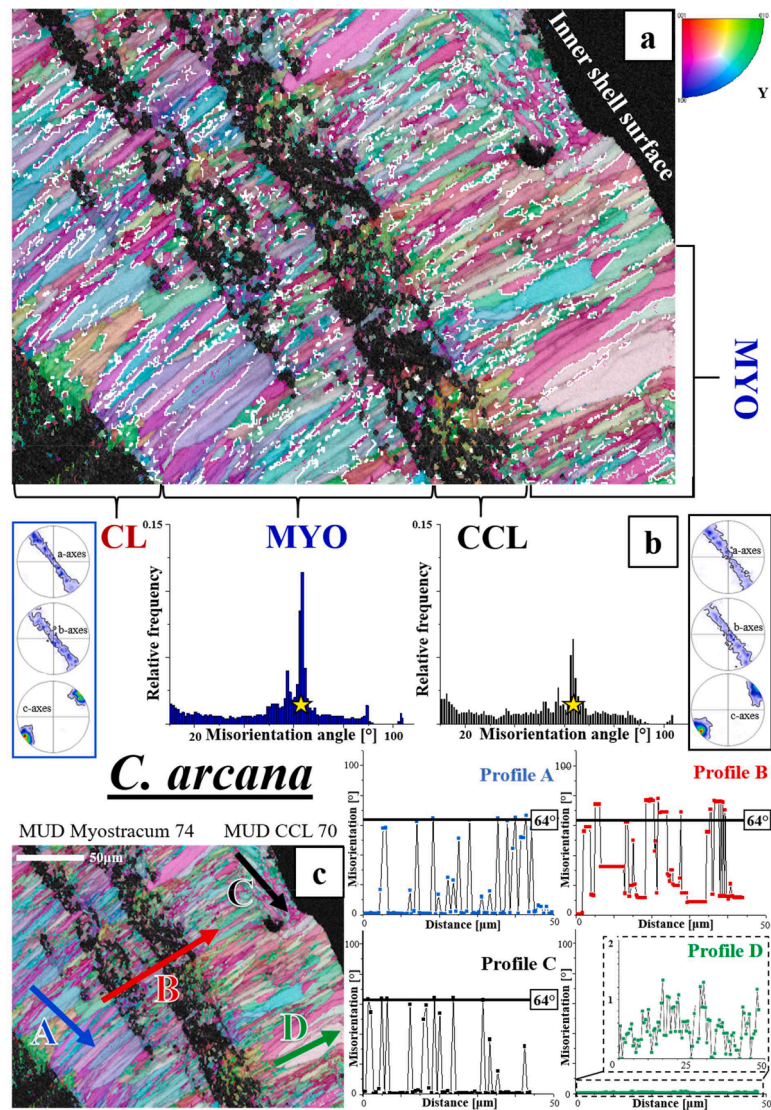
Fig. 10. Misorientation angle analysis of different layers in a transversely sectioned *C. arcana* shell. The EBSD map (a) visualizes the three microstructures that are present in this measurement: The crossed-lamellar layer (CL) in the bottom left and, subsequently towards the inner shell surface, the myostracum (MYO) that is traversed with irregular sheets of complex crossed-lamellar microstructure (CCL). Grain boundary angles between 63° and 65° are highlighted with white points in the EBSD map and indicate twinned aragonite grain boundaries. The misorientation angle plots (b) show myostracum and complex crossed-lamellar layer peaks of varying relative frequency for a misorientation angle of 64° (indicated by yellow stars). The misorientation angle profiles (A–D) traversing the measurement provide further information on the twinning mode in the different structures (b).

or less, 90° to myostracal layers, while in *Chama* first-order lamellae are always at low angles to myostracal layers, occasionally are even almost parallel to the myostracum. The different arrangements of first-order lamellae, relative to the myostraca might contribute to the observed differences between *Glycymeris* and *Chama* in myostracal crystal organisation and texture.

The complex crossed-lamellar microstructure of *Glycymeris* consists of laths that, in general, assemble into first-order lamellae with different crystal orientations (Fig. 1 and [25,26]). For all investigated *Chama* and *Glycymeris* species, we find the latter type of complex crossed-lamellar aragonite at the innermost valve portions (this study and [53]). However, for the fully aragonitic *C. gryphoides*, the aragonite of the ornamentation forms a similar microstructure to the complex crossed-lamellar layer, as defined by Taylor et al. [23]. When cut in cross-section, this microstructure forms a large part of the valve. Due to the applied cut, aragonite crystals in the outermost valve layer appear to be granular to prismatic (Figs. 2b, AP7b) and assemble into differently oriented clusters (Figs. 2b, AP7b). It is striking that this microstructure

occurs at outer shell portions. According to Taylor et al., 1969 and Kennedy et al. [23,39], the complex crossed-lamellar layer forms always the innermost valve regions. Accordingly, we addressed the microstructure of the outer valve layer and ornamentation of *C. gryphoides* as a 'complex crossed-lamellar-type' microstructure.

EBSD measurements allow the determination of crystal co-orientation strength for the different shell layers. We observed, for all investigated species of *Glycymeris* and *Chama*, low crystal co-orientation for complex crossed-lamellar and crossed-lamellar shell portions (*Glycymeris*: MUD (CCL) = 14, MUD (CL) = 11; *Chama*: MUD (CCL) = 26, MUD (CL) = 27). Crystal co-orientation strength for the calcitic ornamentation of *Chama* was increased (MUD = 45 / 55 / 80), relative to that of the aragonitic shell. Most increased, for all investigated species, was the co-orientation strength of aragonite within myostracal layers and individual myostracal crystals (*Glycymeris* MUD myostracum = 67 / 97 / 154 / 133; *Chama* MUD myostracum = 64 / 66 / 51 / 77), relative to aragonite co-orientation of the non-myostracal shell. It has been shown for *G. glycymeris* that individual myostracal prisms are single crystals
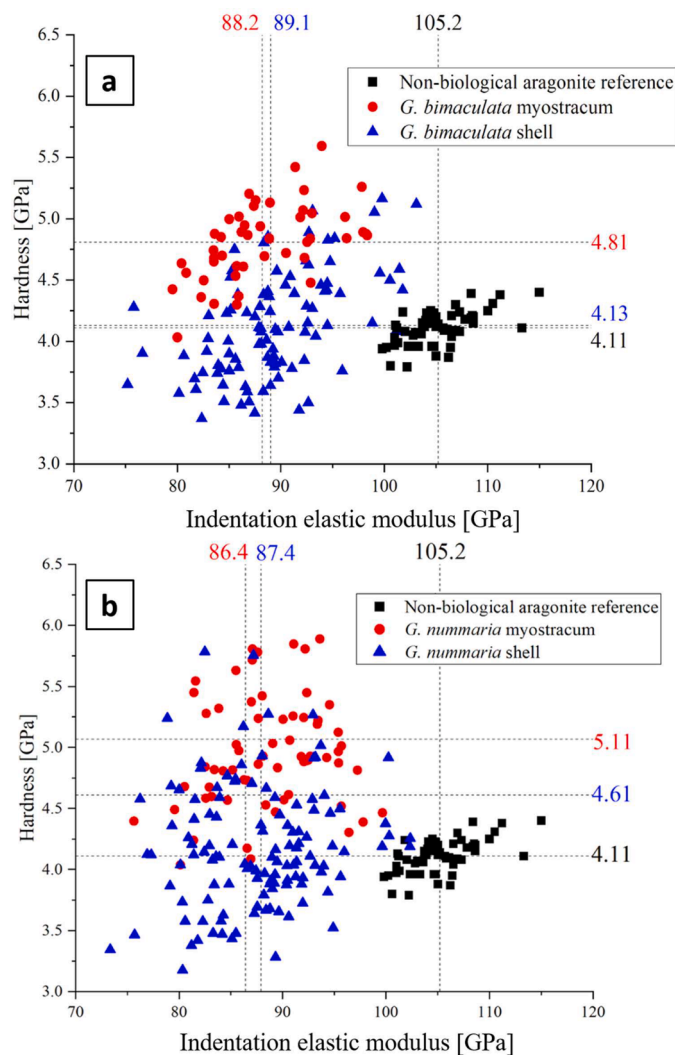
Fig. 11. The hardness and indentation elastic modulus distribution of different layers of *Glycymeris* samples with a geological aragonite reference. Plot (a) depicts that the myostracum layer (red circles) in *G. bimaculata* samples has a distinctly higher hardness than the aragonitic shell (blue triangles) and a non-biological aragonite reference (black squares). The indentation elastic modulus of myostracum and shell is similar and significantly lower than in geological aragonite. Plot (b) depicts the measured values for *G. nummaria*. The highest average hardness is observed in the myostracum. In the shell, despite the large standard deviation, the average hardness is higher than in the geological reference. Similar to *G. bimaculata*, the observed indentation moduli in the *G. nummaria* shell and myostracum are both similar, yet explicitly lower than the non-biological aragonite reference. Crossed-lamellar and complex crossed-lamellar layers are combined as "shell" due to their similar physical properties. The given average values have the following standard deviations σ: Hardness: Reference 0.14, *G. bimaculata* myostracum 0.31, *G. bimaculata* shell 0.39, *G. nummaria* myostracum 0.46, *G. nummaria* shell 0.41. Indentation elastic modulus: Reference 3.2, *G. bimaculata* myostracum 5.1, *G. bimaculata* shell 5.2, *G. nummaria* myostracum 5.6, *G. nummaria* shell 6.0. A breakdown of the individual layers and profile positions can be found in the appendix of this publication (Figs. AP15, AP16).

(Fig. 8a, c, d, e in [25]). We also find this for all species that were investigated in this study. The latter might be an indication that individual myostracal prisms contain very little organic substance. It should be noted that myostracal aragonite of *Chama* is less co-oriented than myostracal aragonite of *Glycymeris*.

4.2. The microstructure and texture of the myostraca

Kennedy et al. [39] and Taylor and Kennedy [68] describe that bivalve myostraca are assemblies of aragonite prisms [39,68]. We observed this as well for *Glycymeris* and *Chama* myostraca, however, based on EBSD measurements, we found further, important, structural characteristics:

(i) Prism morphology regularity/irregularity is different for *Glycymeris* (Fig. 4) and *Chama* (Fig. 5).
(ii) Crystal co-orientation strength within adductor and pallial myostraca is different for *Glycymeris* and *Chama* (Figs. 4, 5).
(iii) Orientational probability density distribution within myostraca is different for *Glycymeris* and *Chama*, with *Glycymeris*, in most cases, showing 3D "single-crystal-like" (e.g., Figs. 4, 6, 7a) and *Chama* exhibiting, very often, axial (fibre) textures (e.g., Figs. 5, 8, 10).
(iv) The aragonite of *Glycymeris* and *Chama* pallial, adductor and pedal myostraca has a microstructure that is characteristic of a crystal growth process derived of growth competition (this study and Crippa et al. [25,26]). Hence, wherever muscles attach to the shell, a hard tissue is formed that has a microstructure that is generated through growth competition. The growth competition process has two important structural effects: (a.) at an advanced stage of the crystallization process, the crystals are large entities. (b.) with progressive growth, a common growth direction develops for all crystals and a specific crystallographic lattice orientation is attained. This is discussed subsequently.

According to Checa [69], crystal formation and assembly by growth competition is, in the biological realm, a process that is fully governed by physical controls and contrasts the processes at the formation of other carbonate biomaterial microstructures. In the latter, microstructure development is determined by biological determinants, such as the influence of organic matrix biopolymers or the influence of the secreting cells when being in direct contact with the forming crystals [69]. Castro-Claros et al. [27] describe for *Ostrea stentina* and *Anomia ephippium*, that adductor myostracal mineralization takes place, among other possible ways, via CaCO$_3$-containing vesicles, which become delivered to the extrapallial space (Fig. 5d, e, h in [27]). This is in contrast to the non-myostracal, portion of the shell (of *Ostrea stentina* and *Anomia ephippium*), where, at secretion, mantle cells are in close contact with the forming biocarbonate (Castro-Claros et al. [27]). Accordingly, different biomineralization processes account for the formation of non-myostracal and myostracal Ca-carbonate biomaterials. In essence, based on our structural results, and, in analogy to the findings of Clastro-Claros et al. [27], we inferred that the formation of *Glycymeris* and *Chama* myostracal and non-myostracal CaCO$_3$ is initiated by different crystal formation and growth determinants, however, both controlled by the secreting cells. Nonetheless, the growth competition process has two important structural effects: (i) at an advanced stage of the crystallization process, the crystals become large entities (up to 50 μm in diameter and 200 μm in length). (ii) with progressive growth, for all crystals, a common growth direction develops and a specific crystallographic axes orientation is attained, with the c-axes being normal to the inner shell surface. This is discussed further subsequently.

Biocrystal formation through growth competition has been reported for species of various marine organism groups, e.g., for *Liothyrella neozelanica* and *Gryphus vitreus* brachiopod columnar calcite [54,70,71], for *Argonauta argo* and *Argonauta hians* cephalopod shell aragonite [72,73], for rotaliid foraminifera shell calcite [55,74] and for *Glycymeris glycymeris* and *Glycymeris nummaria* bivalve myostracal (adductor, pedal) aragonite [25,26]. With this study, we show for *Chama arcana, Chama gryphoides, Glycymeris bimaculata, Glycymeris nummaria* and *Glycymeris pilosa* that adductor and pallial myostracal aragonite forms through growth competition. This study is part of a larger survey of bivalve
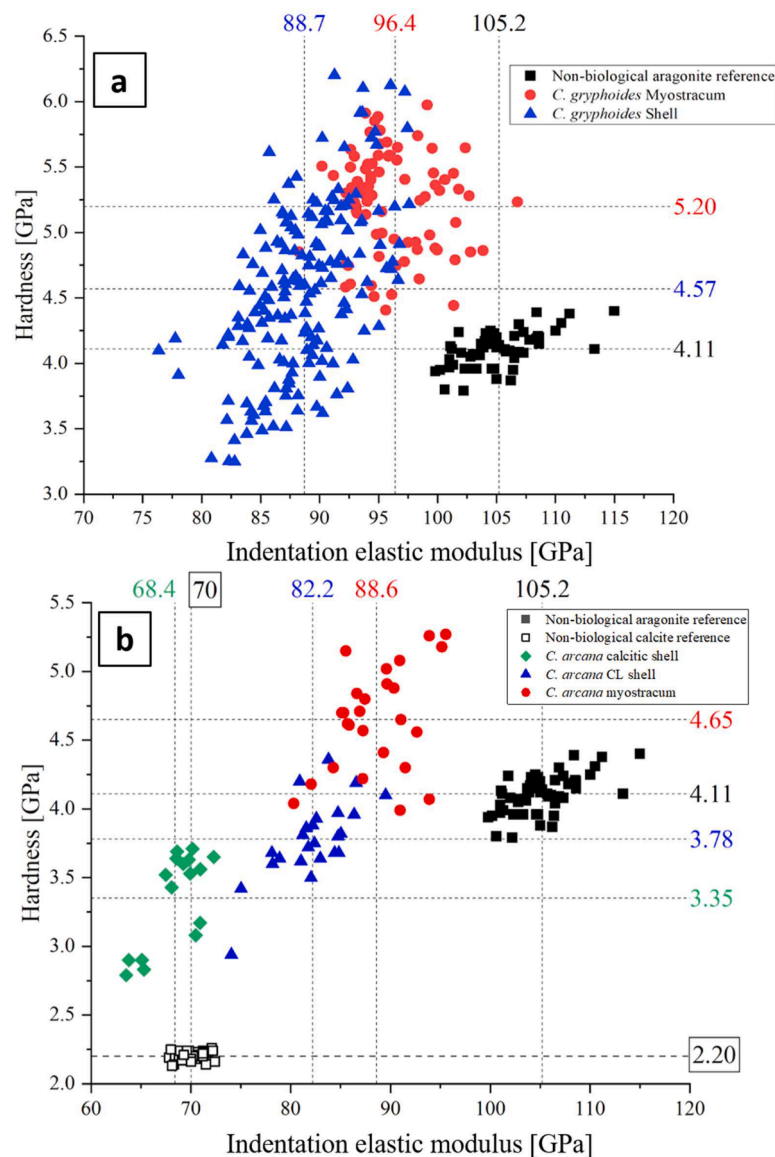
Fig. 12. The hardness and indentation elastic modulus distribution of different layers of *Chama* samples with a geological aragonite reference. Plot (a) depicts that the myostracum layer (red circles) in *C. gryphoides* samples has a distinctly higher hardness than the aragonitic shell (blue triangles) which is slightly harder than non-biological aragonite reference (black squares). While the indentation elastic modulus of the *C. gryphoides* myostracum is lower than the geological reference, the lowest average value was observed for the shell. The second plot (b) indicates the physical properties of aragonitic and calcitic layers in C. *arcana*. The crossed-lamellar layer is only slightly softer than the stiff, non-biological aragonite reference. The myostracum has a significantly higher hardness than the other layers and slightly higher indentation elastic modulus than the crossed-lamellar layer. The calcitic shell is harder than the reference while maintaining a similar indentation elastic modulus. The given average values have the following standard deviations σ: Hardness: Aragonitic reference 0.14, calcitic reference 0.03, *C. gryphoides* myostracum 0.59, *C. gryphoides* shell 0.62, *C. arcana* calcite 0.34*, C. arcana* myostracum 0.38, *C. arcana* CL shell 0.29. Indentation elastic modulus: Aragonitic reference 3.2, calcitic reference 1.26, *C. gryphoides* myostracum 4.4, *C. gryphoides* shell 3.8, *C. arcana* calcite 2.6*, C. arcana* myostracum 3.9, *C. arcana* CL shell 3.5. A breakdown of the individual aragonitic shell layers and profile positions is shown in the appendix of this publication (Figs. AP17-AP19).

myostracal microstructure and texture and covers species of the orders Arcida, Mytilida, Venerida, Unionida, Cardiida, Ostreida, Pectinida, Chamidae and Tellinoidea. For most investigated species we find the competitive-growth-type microstructure for myostracal shell portions, however, we find also different myostracal structures for, e.g. *Mytilus edulis, Arctica islandica, Tellina planata, Venus verrucosa* [75].

One important result of our study is that *Glycymeris* and *Chama* non-myostracal and myostracal aragonite are twinned (Figs. 9, 10, AP14). Crippa et al. [25,26] showed for two *Glycymeris* species that the aragonite in their shells is twinned, for *Chama* we describe twinning of shell carbonate for the first time. We observe polysynthetic, cyclic and polycyclic twinning; for definition see the *Terminology* section of the Methods chapter and [49].

(i) The crossed-lamellar layer exhibits polysynthetic twinning within the two sets, between the third-order laths that form set1 and set2 of a first-order lamella.
(ii) For the myostraca, we find cyclic twinning.
(iii) For the complex crossed-lamellar aragonite we observe poly-cyclic twinning between and within the first-order blocks/lamellae.

Polysynthetic, cyclic, and polycyclic twins are defined by the number of twin planes and their orientation/co-orientation. If twin planes in a twinned crystal are parallel to each other, the twin crystal is termed as a polysynthetic twin; if twin planes in a twinned crystal are not parallel to each other, the twinned crystal is addressed as a polycyclic twin [49].

Table 1

Nanoindentation results for profiles on *Glycymeris* and *Chama* shells. The profiles are shown in Figs. AP14–AP18. (a): absolute values for hardness and indentation elastic modulus in the aragonitic layers, (b) ratios between the absolute values of two aragonitic layers, (c) first and third rows give absolute values, second and forth rows show the ratios between absolute values of the calcitic layer and the non-biological reference.

(a)

	Shell		Myostracum	
	Hardness (GPa)	Indentation elastic modulus (GPa)	Hardness (GPa)	Indentation elastic modulus (GPa)
Glycymeris bimaculata	4.13	89.1	4.81	88.2
Glycymeris nummaria	4.61	87.4	5.11	86.4
Chama gryphoides	4.57	88.7	5.20	96.4
Chama arcana	Aragonite Calcite 3.78 3.35	Aragonite Calcite 82.2 68.4	4.65	88.6

Non-biological calcite
H: 2.20 (GPa) E: 70 (GPa)
Non-biological aragonite
H: 4.11 (GPa) E: 105.2 (GPa)

(b)

Aragonite	Shell vs. Reference		Myostracum vs. Reference		Myostracum vs. Shell	
	Hardness (GPa)	Indentation elastic modulus (GPa)	Hardness (GPa)	Indentation elastic modulus (GPa)	Hardness (GPa)	Indentation elastic modulus (GPa)
Glycymeris bimaculata	1.005	0.847	1.17	0.838	**1.165**	0.990
Glycymeris nummaria	1.122	0.831	1.243	0.821	**1.108**	0.989
Chama gryphoides	1.112	0.843	1.265	0.916	**1.138**	1.087
Chama arcana	0.92	0.781	1.131	0.842	**1.23**	1.078

(c)

Calcite	Hardness (GPa) Shell	Indentation elastic modulus (GPa) Shell	Hardness (GPa) Shell vs. Reference	Indentation elastic modulus (GPa) Shell vs. Reference
Chama arcana	3.35	68.4	**1.523**	0.977

When aragonite crystals are assembled to form the crossed-lamellar arrangement, the first-order lamellae comprise lath-shaped crystals (the third-order lamellae, see Fig. 13b in [26]) that are inclined to each other and alternate in their respective crystal orientations (see Fig. 13a in [26]). For the crossed-lamellar microstructure, we found twin formation mainly between the third-order laths that comprise a first-order lamella (see 64° misorientation boundaries in Fig. 9a) and to a lesser extent between the lamellar sets.

When aragonite is assembled to form the complex crossed-lamellar arrangement, several, irregularly shaped and variously oriented, first-order blocks/lamellae are formed. The latter consist of third-order laths and crystals. For the complex crossed-lamellar microstructure, we observed polycyclic twin formation within the blocks/lamellae and to a lesser extent between them (Fig. 9a). Accordingly, for the complex crossed-lamellar microstructure we detected a high density of 64° misorientations (see Figs. 9a, b, AP15a).

Myostracal (adductor, pallial, pedal) aragonite is cyclically twinned. The 64° misorientations are between adjacent prisms and not within the prisms (Figs. 9a, 10a, AP15a, AP16a). The distinct peak of 64° in the relative frequency–misorientation angle diagram for the myostracum (see Figs. 9b, 10b, AP19b) is, to some extent, due to the low number of total grain boundaries imposed by the large prism size in the adductor myostracum.

4.3. The changeover from non-myostracal, valve, to myostracal crystals

For *Glycymeris* and *Chama,* the transition between the layers of the non-myostracal and myostracal valve portions is continuous. We discuss first the transition from the crossed-lamellar valve to the adductor myostracum and, subsequently, the transition from the pallial myostracum to the complex crossed-lamellar valve portion (Figs. 6 to 8, 9a, 14, 15 and AP14a, c)

Our EBSD results showed that adductor and pallial myostraca form via two crystallization processes:

(i) the *very first crystals* form through epitaxial growth onto the crossed-lamellar template
(ii) *further growth* is guided through the competitive growth process

For *Glycymeris* and *Chama*, the adductor myostracum is always attached to the crossed-lamellar valve portion (Figs. 6, 7a, 8a, 14a to d), while the pallial myostracum attaches to the crossed-lamellar layer, along its external surface, and to the complex crossed-lamellar microstructure, along its internal surface (Figs. 7, 8b, 9a, 14e).

Crystal orientation measurements demonstrated, for the **crossed-lamellar** – adductor **myostracum** changeover, that crystal size and morphology are not transmitted to the myostracum (Fig. 14a). However, the lamellar habitus of the crossed-lamellar structure, thus, crystal orientation of the two sets of first-order lamellae, is transmitted and can be well traced within the adductor myostracum (Figs. 6a, 7a, 14a, b, c). Some crystallographic aspects of the crossed-lamellar texture are also transmitted to the adductor myostracum. Hence, crystallographic axes orientation is conferred from crossed-lamellar to adductor myostracal aragonite. Fig. 14d, e show that the very first-formed adductor myostracal crystals grow epitaxially onto the crystals of the first-order lamellae of the crossed-lamellar layer. At this stage of myostracal growth, all crystal orientations of the crossed-lamellar valve are also maintained within the adductor myostracum. With further growth of the myostracum (controlled by the competitive growth process), this changes, as (i) only some orientations of the crossed-lamellar valve are retained and (ii) a new crystal orientation along the a- and b-axes is developed within the adductor myostracum (Fig. 14f). This newly developed orientation is cyclically twinned, relative to the crystal orientation of the first-order lamellae, and is retained for the entire myostracal growth sequence. The c-axis orientation of the crystals with the new crystallographic orientation is parallel to the c-axis orientation
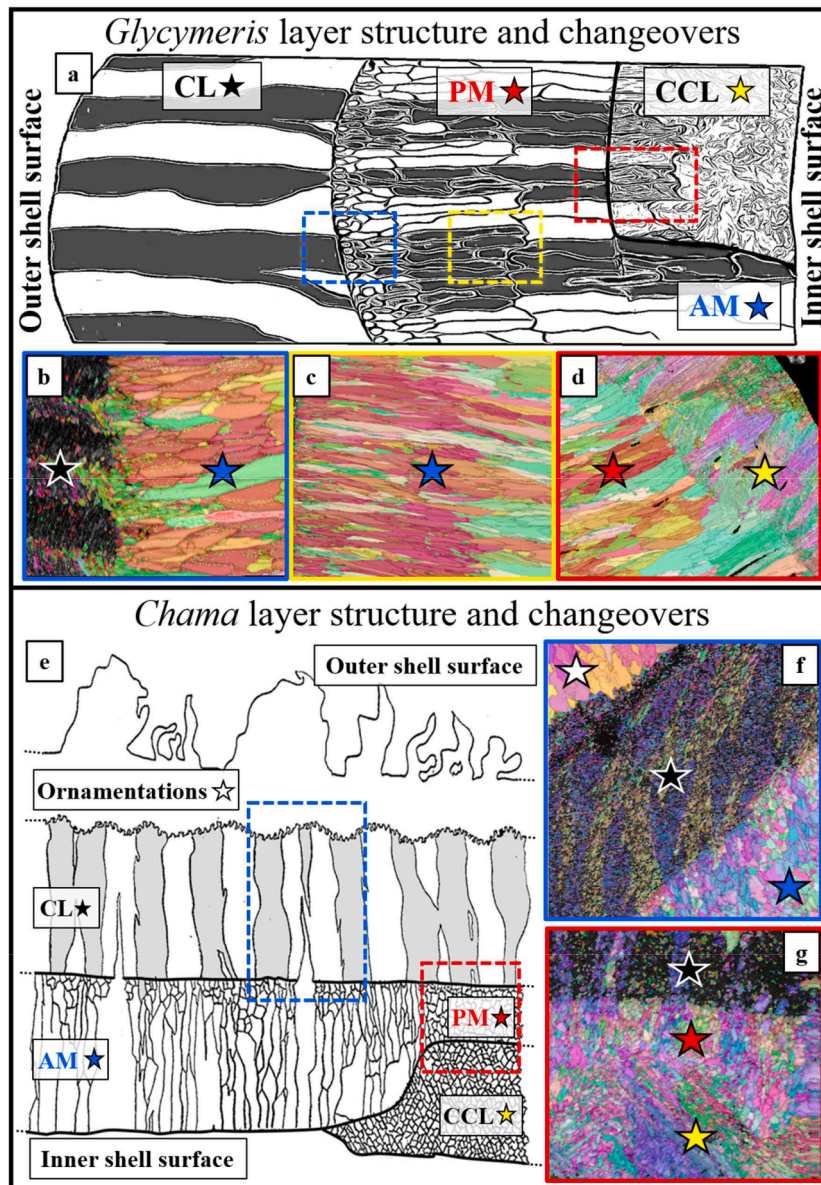
Fig. 13. Schematic illustrations depicting the general layer structure and transitions of *Glycymeris* (a–d) and *Chama* (e–g) shells. The outer valve layer of investigated *Glycymeris* samples has a crossed-lamellar microstructure (black star in b). The crystal orientation pattern is transmitted (b) and continued (c) in the subsequent, competitively grown adductor and pallial myostracum layers (blue and red stars in b–d). At the changeover between the pallial myostracum and complex crossed-lamellar layer (yellow star in d), the large protruding myostracal prisms exhibit extensive polycyclic twinning. While ornamentations in *C. gryphoides* are aragonitic, in *C. arcana* shells, the ornamentations are calcitic (white star in f), and form a three-dimensional interlocking mechanism with the subsequent crossed-lamellar layer (black star in f). The crossed-lamellar crystal orientation is transmitted into the myostracal crystals (blue star in f, red star in g). While the orientation transmitted by pallial myostracum crystals devolves in the first μm of the complex crossed-lamellar layer (yellow star in g), it is eventually lost in the convoluted microstructure of the complex crossed-lamellar layer.

of crystals of the first-order lamellar sets and to the c-axis orientation of the epitaxially-formed adductor myostracum crystals (see pole figures in Fig. 14d–f). This indicates that the restrictions of the polysynthetic twinning in the crossed-lamellar layer no longer apply to the myostracum. Hence, c-axis orientation of all crystals (i) remains similar for the different microstructures (crossed-lamellar and myostracal), (ii) become oriented in parallel along inner shell layers and (iii) is perpendicular to the inner shell surface. (iv) Crystal co-orientation strength is low for the first-formed crystals of the myostracum, however, for the crystals that nucleate on the crossed-lamellar template, crystal co-orientation strength increases significantly towards inner shell surface. (v) The restrictions of polysynthetic twinning within the third-order lamellae of the crossed-lamellar layer are not continued in the adductor myostracal layer. It should be kept in mind that all these structural characteristics

and effects are initiated by the competitive growth process.

In summary: (i) the first crystals of the adductor myostracum grow epitaxially onto the crossed-lamellar template (Fig. 14a, d, e). (ii) further growth of myostracal aragonite is controlled by growth competition. (iii) two c-axes orientations, one for each set of first-order lamellae (see [20,25,26]) and two different a- and b-axes orientations are transferred to the adductor myostracum. (iv) c-axis orientation remains rather conservative for the crossed-lamellar and the adductor valve portion, while a new a- and b-axes orientation develops within the myostracal layer. (v) for the crossed-lamellar layer we find polysynthetic twinning within the first-order lamellae and, only to some extent, twinning between the two sets.

Pallial myostraca are, in 3D, sheet-like structures [76,77] that are incorporated into the valves and separate adjacent hard tissue layers,
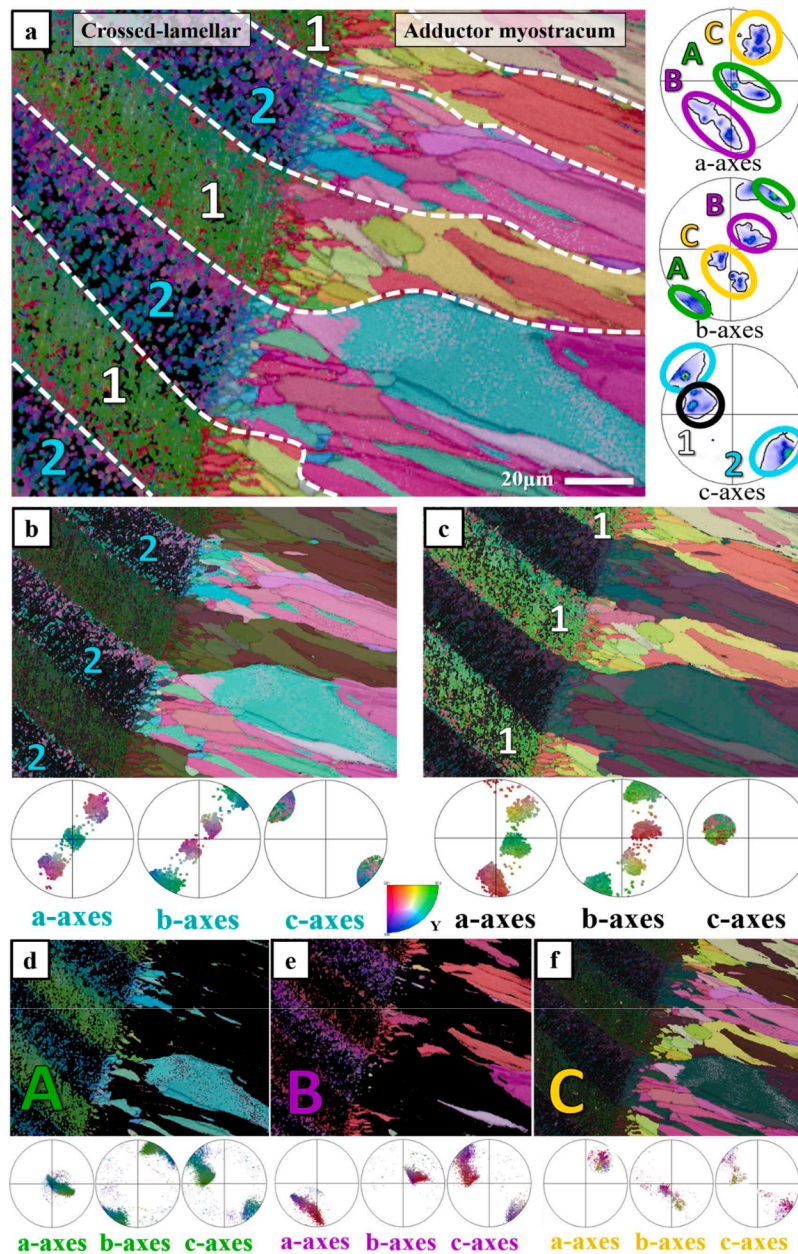
Fig. 14. Breakdown of crystallographic texture in the non-myostracal, valve-myostracum changeover portion of a transversally sectioned *G. pilosa* shell. The transmission of the set1 and set2 crystal orientation pattern into the adductor myostracum is highlighted in EBSD maps and pole figures for the entire dataset (a) and various subsets (b–f). The pole figures a-c show that the aragonite c-axes in first-order lamellae set 1 are tilted, relative to aragonite c-axes in set 2 that run almost parallel to the direction of crystal growth. In addition to the two twinned orientations inherited by each of the two first-order lamella sets (d, e), the competitive growth process initiates a third, unique, orientation that is found only in the myostracum and differs in orientation of the a- and b-axes (f). The latter corresponds to the third orientation of the polycyclic twin.

having specific microstructures [39]. For *Glycymeris* and *Chama*, the pallial myostracum connects, along its outer surface to the crossed-lamellar (Figs. 8b, 9, 15) and along its inner surface to the complex crossed-lamellar microstructure (Figs. 7b, 8b, 15). Figs. 9 and 15 visualize the corresponding transitions between the microstructure of the pallial myostracum and the two different, non-myostracal valve layers.

(i) The changeover from the crossed-lamellar valve to the pallial myostracum

As is the case for the changeover from the crossed-lamellar valve portion to the adductor myostracum, the lamellar habitus of the first-order lamellae and the polysynthetic twinning pattern are transferred from the crossed-lamellar valve to the pallial myostracum. These two structural characteristics continue across the entire extent of the pallial myostracum (see white arrows in Fig. 15a). As is the case for the adductor myostracum, for the pallial myostracum as well, we observed within the pallial myostracum the generation of an additional crystal orientation of the a- and b-axes (Fig. 15b–d). It appears that this is the third orientation of the polycyclic twin previously restricted by the mantle. The latter controlled the crossed-lamellar crystal growth, prior to pallial muscle attachment (Fig. 15d). When based on c-axis orientation, the two orientations of the two first-order lamellar sets carry over from the crossed-lamellar to the complex crossed-lamellar valve portion. Hence, overall, six different aragonite crystal orientations are developed
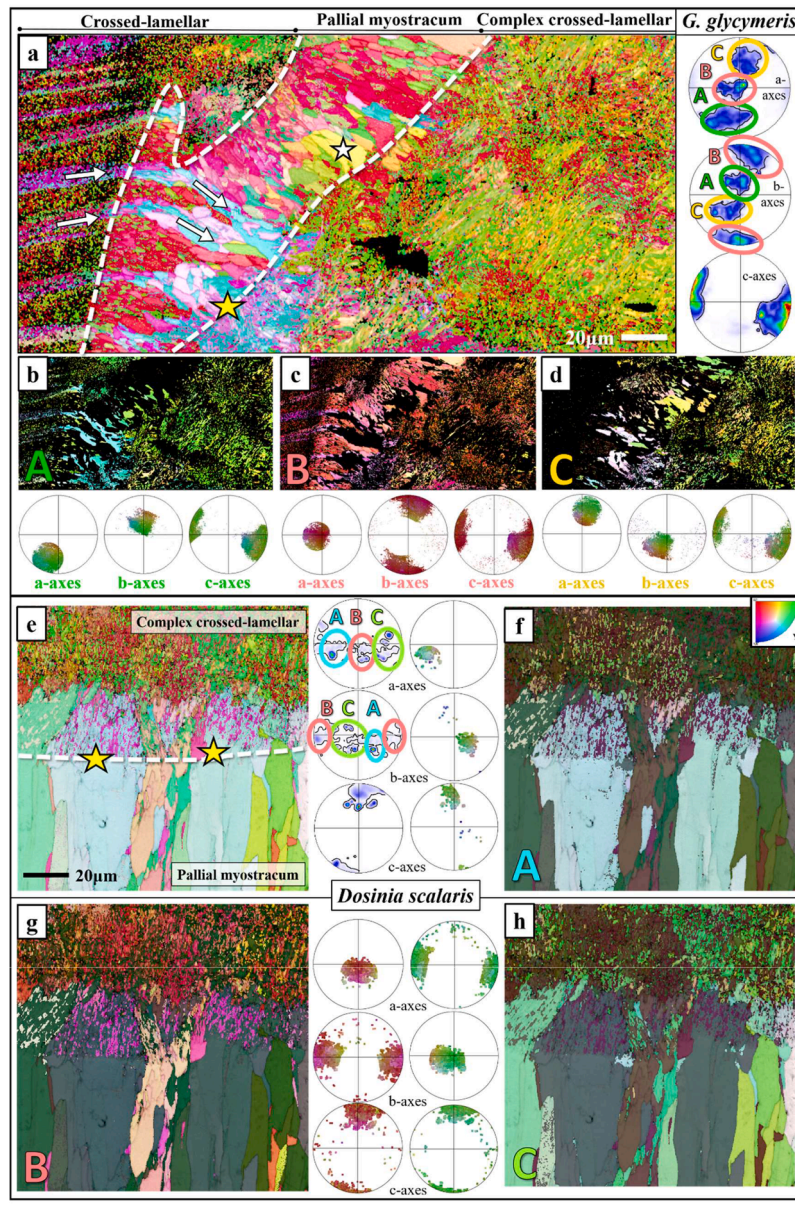
Fig. 15. Breakdown of the crystallographic texture in the non-myostracal valve-myostracum changeover region of an obliquely sectioned *G. glycymeris* shell and a transversally sectioned *D. scalaris* shell. In *G. glycymeris*, the crossed-lamellar crystal orientation pattern continues through the pallial myostracum (white arrows in a) and appears to extend into the complex crossed-lamellar layer (b, c, white star in a). Similar to Fig. 12, a unique set of orientations, that was not transmitted from the texture of the first-order lamellae, is generated in the myostracum and continues into the complex crossed-lamellar layer (d). Similar to Fig. 7b, at the changeover from pallial myostracum to the complex crossed-lamellar layer a sharp boundary of incipient polycyclic twinning is visible in *D. scalaris* (white stars in e). The 3D "single-crystal-like" crystallographic texture comprises three sets of orientations (f–h) that are generated by the orientation pattern of first-order lamellae and the competitive growth mechanism of the myostracum.

up to the transition from the pallial myostracum to the complex crossed-lamellar layer. They correspond to the two sets of first-order lamellae imposed by the crossed-lamellar layer and the two orientations resulting from polycyclic twinning.

(ii) The changeover from the pallial myostracum to the complex crossed-lamellar valve

Figs. 7b and 15e–h show close-ups of the transition from the pallial myostracum to the complex crossed-lamellar shell. The white dashed line in Fig. 15e indicates the border between myostracal and complex crossed-lamellar layers. We observed the following: (i) The crystals of the complex crossed-lamellar layer (yellow stars in Figs. 7b, 15e) grow epitaxially onto the previously formed myostracal crystals. The

prismatic microstructure and the formation of large prisms are carried over from the pallial myostracum into the complex crossed-lamellar valve portion (yellow stars in Figs. 7b, 15e). For the latter transition from one microstructure into the other, we observed similar structural characteristics as detected for the transition from crossed-lamellar to pallial myostracum. We found again epitaxial growth of the first-formed crystals of the complex crossed-lamellar, non-myostracal, valve portion onto the prisms (large prisms that form at an advanced stage of crystallization) of the pallial myostracal template. For the complex crossed-lamellar layer we have detected for both, *Glycymeris* and *Chama*, polycyclic twinning. Extensive polycyclic twin formation is started right at the transition from pallial myostracum to the complex crossed-lamellar shell (yellow stars in Figs. 7b, 15e) and executed throughout the entire inner shell layer.
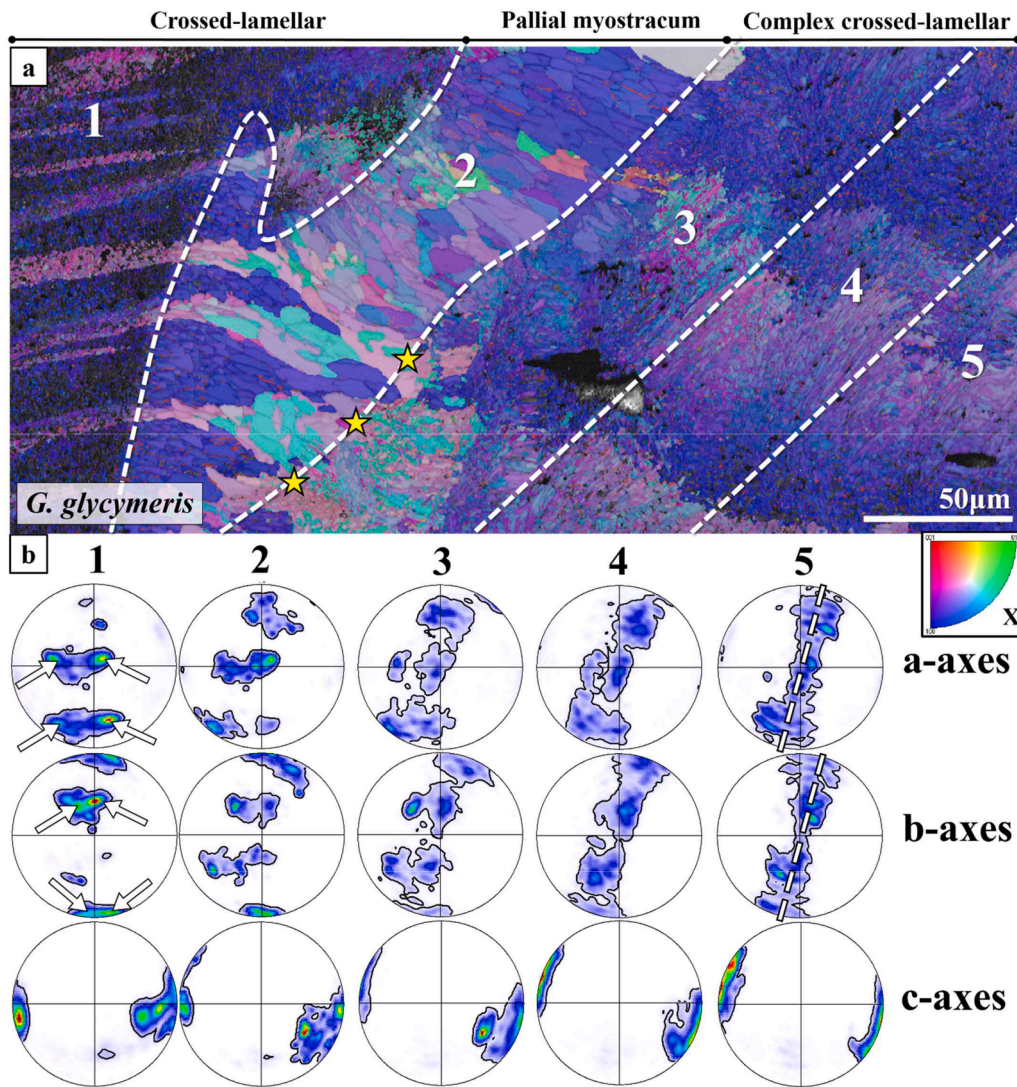
Fig. 16. Texture evolution for *G. glycymeris* from the crossed-lamellar (1) via the pallial (2) to the complex crossed-lamellar (3, 4, 5) microstructure, respectively. The measurement is split into five sections, indicated by a white dashed line in the EBSD map (a). The first pole figure (b1) corresponds to the crossed-lamellar layer, the second (b2) to the pallial myostracum and pole figures three to five (b3–5) to different stages of the complex crossed-lamellar layer (b). The pole figure (b1) indicates that the crossed-lamellar layer comprises two sets of orientations, each with a slightly deviating c-axes orientation. This pattern is continued into the pallial myostracum (pole figure b2), however, here an additional a- and b-axes orientation is added through polycyclic twinning, as described in Fig. 15. While the myostracal texture is initially continued into the first few μm of the complex crossed-lamellar layer (as visible from the EBSD map and pole figure b3), the single crystal-like texture (pole figures b1, b2) gradually transforms into an axial/fibre texture (pole figures b3, b4, b5). This indicates that the initial lamellar crystal orientation pattern of the crossed-lamellar shell is kept in the pallial myostracum, but it is abandoned in the advanced growth stages (parts 4 and 5) of the complex crossed-lamellar layer.

The different twinning modes impact the texture of the pallial myostracum and of the complex crossed-lamellar shell layers. We visualized with pole figures (Fig. 16) the transformation from a 3D "single-crystal-like" to an axial texture. Originating in the crossed-lamellar valve, it is modified in the pallial myostracum and transforms into an axial texture in the complex crossed-lamellar shell. Fig. 16 depicts the mode of crystal arrangement with an EBSD map (Fig. 16a) and corresponding pole figures (Fig. 16b), covering the crossed lamellar, pallial myostracal and complex crossed-lamellar layers. Numbers 1 to 5 indicate chosen segments of the map and the corresponding pole figures: 1: crossed-lamellar valve, 2: pallial myostracum, 3: complex crossed-lamellar valve portion directly next to the pallial myostracum, 4 and 5: complex crossed-lamellar portions further away from the myostracum. The pole figure of the crossed-lamellar layer shows four orientation probability maxima for the a- and b-axes (see arrows in pole Fig. 1 in Fig. 16b). These correspond to the inclination between the two sets of

first-order lamellae and the two, polysynthetically twinned, crystal orientations within each set of a first-order lamella. Due to these maxima, the pole figure of the crossed-lamellar shell conveys a single crystal-like texture. This texture is transferred into the pallial myostracum, however, in the pallial myostracum a third "set" of twinned orientation develops. The latter indicates, most likely, the loss of biological control over aragonite crystal growth during adductor muscle attachment. Most probably, it is not induced on purpose but is rather accidental (pole Fig. 2 in Fig. 16b). The pallial myostracum texture is transferred to the first-formed portion of the complex crossed-lamellar layer, the layer directly adjacent to the pallial myostracum, (pole Fig. 3 in Fig. 16b and see Section 3 in the EBSD map), however, the density maxima (see pole Fig. 3) are less distinct due to the polycyclic twinning mode in the complex crossed-lamellar layer. Further away from the pallial myostracum, towards inner shell surface (map segments 4, 5 in Fig. 16a and pole Figs. 4 and 5 in Fig. 16b), the texture becomes more and more axial

as the c-axes of the lamellar sets merge to a common c-axes orientation (pole Fig. 5 in Fig. 16b), that is normal to inner shell surface.

In summary: (i) We observed that both adductor and pallial myostraca have similar structural characteristics. (ii) We observed for both changeovers, from the crossed-lamellar valve to the adductor or pallial myostracum and from pallial myostracum to the complex crossed-lamellar valve, similarities in transmission of crystal orientation, utilization of epitaxial growth and twin formation. (iii) We found significant structural differences between the non-myostracal, valve, and myostracal layers. The above-discussed structural features have not yet been described elsewhere.

4.4. The hardness and indentation elastic modulus of myostracal and valve aragonite

Table 1 and Figs. 11, 12 highlight, for the investigated *Glycymeris* and *Chama* species, that myostracal valve sections are harder, in comparison to the non-myostracal valve layers and to non-biological aragonite. Concerning indentation elastic modulus, non-myostracal valve and myostraca show comparable values, although, we find species (*C. gryphoides* and *C. arcana*) where myostracal indentation elastic modulus is slightly increased, relative to the indentation elastic modulus of the valves.

Is hardness and indentation elastic modulus compared between myostracal, crossed-lamellar, complex crossed-lamellar aragonite arrangements, we found that, on average, myostracal hardness is increased by 15 % and myostracal indentation elastic modulus by 5 %, relative to the hardness and indentation elastic modulus of the microstructures of the non-myostracal valves. Zhao et al. [78] made nanoindentation measurements on the adductor myostracum of the fast-swimming scallop *Placopecten yessoensis*. Adductor myostracum hardness and indentation elastic modulus are 5.65 GPa and 78.03 GPa, respectively, while hardness and indentation elastic modulus values for the non-myostracal valve are 4.33 GPa and 69.76 GPa, respectively [78]. The material property results for *Placopecten* compare well with our material property measurements on *Chama* and *Glycymeris*. Hence, irrespective of the lifestyle of the bivalve (sessile, burrowing or swimming), we observed for the myostraca an increased hardness and a slightly increased indentation elastic modulus relative to the hardness and indentation elastic modulus values that are measured for the respective non-myostracal valve.

Variations in the chemical composition of aragonitic biominerals can affect their mechanical response [79]. However, *Chama* and *Glycymeris* shells share similar chemistry, thus, the question is, what initiates myostracal hardness? Two factors are conceivable: (i) generally, material hardness is related to crystal twinning [80–83], as twin boundaries block dislocation and crack propagation and induce delocalization of deformation around the crack tip. Another effect of twinning is the reduction of crystal sizes due to formation and incorporation of additional, new, grain boundaries. In inorganic materials, smaller grain sizes lead to increased hardness due to the Hall-Petch relation [84–87]; however, our results show superior hardness values for the microstructure with the largest prisms. Furthermore, we find twinning in all three layers and the exact correlation between twinning and the measured physical properties is uncertain due to the small probe size with respect to the large twin domains.

(ii) The more feasible explanation involves the proportion of mineralized material to organic matter and their distribution within the layers. For *Chama* and *Glycymeris*, myostraca consist of assemblies of large, strongly mineralized, prisms, while other valve portions are formed of assemblies of minute, organic substance-coated, laths. Myostracal prisms are also encased in organic matter; however, they are significantly larger mineral entities in comparison to the laths. The observed increase in myostracal hardness values, thus, can be explained by the increased mineralization of myostracal prisms and the relatively low amount of organic matrix material that surrounds the crystals. The latter prevents indented grains from shifting and rearranging in softer organic matter and leads to a higher measured hardness. To account for crystal anisotropy that can influence the physical properties of a material [88,89], the layers were indented both parallel and perpendicular to the c-axes orientations. For both cases, the myostracum layer shows higher hardness values than the non-myostracal valve (see also [90]).

4.5. The effect of myostracal crystal organisation

The topological relation between mollusc muscles and myostracal hard tissue is well-investigated by now (e.g. [27,58,91–95]). The muscle tissue does not connect directly to myostracal carbonate or insert into myostracal hard tissue. Muscle cells terminate at the basal cellular membrane of a layer of specialized epithelial cells, the tendon cells (e.g. [27,92,93]). As described by other studies (e.g. [58,92,93]), the tendon cell layer has hemidesmosome junctions at its basal and apical sides, contains actin, myosin and paramyosin microfilament bundles and has, at its apical side, knob-like microvilli. The microvilli are close to myostracal crystals, however, do not insert into these. A seam of extracellular polymer fibrils, collagen fibrils, derived from or/and connected to the microvilli (e.g. [93,95]) is the substance that is directly next to myostracal crystals and, even more important, enters into the basal side of the prisms (e.g. [27,93–95]). Thus, muscle fibres connect to myostracal crystals via the basal tendon cell layer [93] and the extracellular actin, myosin and paramyosin fibrils in the myostracal aragonite [58]. Hence, bivalve myostracal prisms are biopolymer fibre-reinforced polymer-mineral composites.

The opening and closing of mollusc valves is an interplay between adductor muscle and hinge ligament action [96,97]. Contractile activity of the muscles closes the valves, causing the ligament to bend and compress. During muscle relaxation, this energy stored in the ligament opens the valves (e.g. [63,64]). Bivalve adductor muscles are among the strongest muscles known for invertebrates and vertebrates [27,58]. Bivalve adductor muscles can generate tensions up to 15 kg/cm^2 to counteract the force of the ligament, which, in some bivalves, takes 1 kg/cm^2 or more [58]. The strong forces that bivalve muscles can exert are achieved through (i) the use of a combination of different muscle types and muscle fibre structures (e.g. thick, thin muscle filaments; striated, smooth muscles [58,63]), (ii) a tight connection from muscle to myostracal tissue (e.g. variation in muscle cross-section [63,66,98,99]) and (iii) the integration of tendon cell-derived biopolymer fibrils into myostracal crystals. From a material property perspective of particular interest is the junction between the apical surface of the tendon biopolymer fibrils and the basal surface of the myostracal crystals. As very dissimilar materials join at this junction, interfacial stress is likely to accumulate here and will lead to fracture. However, Zhao et al. [78] reported for the scallop *Placopecten yessoensis* that, at forcing the valves apart, rather the adductor muscle itself breaks into half, instead of being torn away from the myostracal crystals. Hence, as the biopolymer fibrils of tendon cells are anchored within the myostracal crystals, much less interfacial stress accumulates at the fibril-crystal interface. Accordingly, the incorporation of the fibrils into the crystals is the decisive factor for the strength of the myostracum-tendon layer connection.

Myostracal crystals are always aragonitic (e.g., this study and [25,53, 90,100]). Even in entirely calcitic shells, e.g. that of Ostreoidea, myostraca are aragonitic [101]. This might have the following reasons: (i) it is well-documented by now for nacreous and coral aragonite that biologically formed aragonite has biocompatible properties [102–105]. Hence, in analogy, we can assume that this strong preference for molluscs to produce myostracal crystals solely of aragonite might be rooted in the biocompatible nature of the bioaragonite. (ii) The high Mg^{2+} content in many marine environments due to the large Ca^{2+} consumption [106] may slow down the growth kinetics of calcite, thus, thermodynamically favouring aragonite formation in oceanic environments [107,108]. (iii) The competitive growth process initiates that large and specifically oriented prisms are adjacent to tendon cell filaments. Hence,

a specific crystallographic face of aragonite crystals borders filament ends. This might foster attachment and incorporation of the biopolymer filaments into myostracal aragonite.

The pallial, adductor (this study) and pedal myostraca [25] of bivalve species that were, so far, investigated with EBSD have a competitive growth-derived microstructure. The result of the latter crystal growth process is that (i) aragonite crystals become oriented in a specific direction and (ii) large crystals face the array of organic fibrils and the apical surface of the tendon cell layer. Tompa and Watabe [93] and Castro-Claros et al. [27] discussed and showed that the tendon cell-associated extracellular polymer fibrils insert into myostracal crystals. Through competitive growth, the basal surface of myostracal crystals becomes oriented in parallel to the apical surface of tendon cells. Consequently, with the adductor myostracum – tendon cell – muscle fibre constellation aragonite c-axis orientation is parallel to the morphological, long axes direction of organic fibrils (see pole figures in Figs. 4 and 5) and the orientation of aragonite prisms becomes aligned with the direction of the tensile force. Thus, the myostracal microstructure appears to be beneficial for embedding polymer fibres into crystalline materials, as it results in a huge increase in tensional force. However, it is not yet clear, whether this crystal arrangement is derived solely from the lack of cellular control during crystal growth or is due to biological adaptations. For *Anomia ephippium* it has been shown that collagenous fibrils are arranged in parallel within myostracal prisms (personal communication C. Salas), however, the exact mechanism that initiates the arrangement is, for biologically secreted hard tissues, not yet well understood. For non-biological, polymer fibre–ceramic materials it is shown that the latter can sustain the highest tensional forces when the incorporated polymer fibres are oriented within the crystals in parallel [109,110]. As bivalve adductor and catch muscles are among the strongest muscles known for organisms, exceeding significantly tensile forces of vertebrate muscles [58], a parallel alignment of biopolymer fibrils within the orchestrated aragonite prisms is most likely (e.g. personal communication C. Salas). Hence, the competitive growth mechanism secures, for the organic fibril–crystal attachment, the right topological relationship between crystals, on one hand, and polymer fibrils, tendon cells, on the other.

4.6. Is strength and mode of valve action relatable to the size, form, and structure of the adductor myostracum?

Yonge [97] suggested that the size, structure and combination of muscle types of mollusc adductor and pedal muscles should be relatable, at least to some extent, to the environment. It is comprehensible that the frequency, speed and duration of valve opening and closure have to be connected to the lifestyle and habitat of the organism.

The many studies on mollusc muscle action show that there is a range of speeds of muscle contraction and relaxation and that these depend on the specific need for muscle utilization. Hence, variation in muscle contraction and relaxation must be paralleled and observable by muscle structure [63,98,99,111,112]. Depending on the respective mode of the bivalve's lifestyle (being sessile, burrowing or swimming), the striated or smooth muscle fibres might be developed differently, as a response to the different functional demands of the animal [113,114]. Accordingly, variations in the adductor (muscles that close the valves) and pedal (muscles that move the foot) muscle structure might influence the development, size, and crystal arrangement pattern of the muscle imprints, the myostraca.

In our study, we compared adductor myostracal structure, microstructure, texture and material properties of sessile and burrowing species belonging to different bivalve orders. We have deliberately chosen organisms that form thick valves. We complemented our results and discussion with one EBSD measurement made on the adductor myostracum of the swimming bivalve, *Placopecten magellanicus* (Fig. AP21). The latter species is one of the strongest swimmers among bivalves. *P. magellanicus* is a scallop and only has the posterior adductor

muscle. Nonetheless, we found:

(i) a marked difference in the dimension of the adductor scars. The swimming bivalve species developed the largest adductor scar, relative to the adductor scars of the burrowing and the sessile species. As the scar of the swimming *P. magellanicus* is large in extent, one can differentiate for its adductor scar microstructure (the latter measured with EBSD) between imprints initiated by phasic and by tonic muscles, hence, imprints generated by striated and smooth muscles [112].

(ii) significant differences in myostracal prism morphology regularity. The sessile *Chama* species form their adductor myostracum with strongly irregularly-shaped prisms, relative to prism morphology developed by the swimming *P. magellanicus* and the burrowing *Glycymeris* species.

(iii) differences in prism size. This can be well investigated for those bivalve species that form even prism morphologies. The myostracum of the swimming *P. magellanicus* consists of many, very thin, regularly shaped prisms (see Fig. AP21), while the adductor prisms of the burrowing *Glycymeris* species are also regular in shape, but significantly thicker (e.g., Fig. 4b).

Nonetheless, common to all investigated bivalves, irrespective of their lifestyles and habitats, is the development of the competitive growth microstructure for myostracal aragonite. It develops large prisms close to the row of tendon cells, orientation of c-axes normal to the inner shell surface and alignment of aragonite c-axes parallel to the long axis of the extracellular biopolymer fibrils that are associated with the tendon cells. Hence, for the investigated species, myostracal microstructure, texture and material properties are (i) to a large extent determined by the physical competitive growth process that results from the mantle losing control over crystal growth. However (ii), the investigated *Chama* and *Glycymeris* samples exhibit differences in the organisation and texture of the myostracum, including crystal morphologies, thickness, and continuation of the crossed-lamellar orientation pattern. These might be related to the structure of the attached muscles, which is modulated by environmental factors, such as the lifestyle of the bivalve, and the ligament size and strength. Opening and closing the valves is an integrant within the interplay between the resilience and efficiency of the hinge ligament and the resilience and efficiency of the adductor muscle [40,43,111,112,115,116].

5. Conclusions

The bivalve shell has several functions. It protects the soft tissue of the organism, is involved in the different modes of animal movement (swimming, burrowing, sedentariness) and acts as a skeleton for the attachment of muscles. It also may have hydrodynamic functions related to feeding. The bivalve shell consists of diverse arrangements of well-ordered crystals (microstructures). These comprise all mineralized shell layers, including the myostraca. Nonetheless, despite significant differences in shell microstructure, for the investigated species, we find only two texture patterns. In most cases, the preferred crystallographic orientation (texture) is axial, in some it is three-dimensional "single-crystal-like".

In this contribution, we highlight and discuss differences in valve and muscle attachment site crystal organisation for bivalve species following different lifestyles and living in different environments. From our structural and material property results, we conclude the following:

1. For *Chama* and *Glycymeris*, non-myostracal, valve and myostracal crystal size, type and assembly pattern are distinct. Contrary to the crossed- and complex crossed-lamellar arrangements, pallial and adductor myostracal crystals have an organisation pattern that is characteristic of a crystal assembly mode obtained through growth competition. The assembly of non-myostracal, valve crystals is

governed by biological, the assembly of myostracal crystals mostly by physical processes, respectively.

2. For *Glycymeris* and *Chama* the adductor myostracum is attached to the crossed-lamellar microstructure, the pallial myostracum is between the crossed- and the complex crossed-lamellar crystal assemblies. Crystal size and morphology are not transferred from the crossed-lamellar microstructure to myostracal layers/portions. The laminated appearance of the crossed-lamellar valve as well as crystal (c-axis) orientation and the twinned nature of the aragonite become transmitted from valve to myostracal layers.

3. For the investigated bivalves, crystallographic texture gradually shifts from a three-dimensionally ordered preferred orientation ("single-crystal-like") in the crossed-lamellar layer to an axial orientation in the complex crossed-lamellar layer. In *Chama*, the pallial myostracum shows, in most cases, an axial texture, with a- and b-axes orientations distributed homogeneously on a great circle. In the pallial myostracum of *Glycymeris,* a 3D "single-crystal-like" texture is visible. For the latter, the six density distribution maxima of aragonite crystal orientation in the pole figures can be attributed to cyclic twinning.

4. The first-formed myostracal crystals nucleate epitaxially onto the aragonite of the crossed-lamellar microstructure. The crystallographic orientation of valve and myostracal (adductor, pallial) crystals is parallel, it is, thus, transferred from one layer to the other. At slightly advanced stages of myostracal growth, in addition to the aragonite orientation of the first-order lamellae, a further crystal orientation develops within the myostracum and is kept for all additional growth stages. The competitive growth mode of myostracal crystals ensures that aragonite c-axes become oriented normal to inner shell surfaces.

5. Bivalve muscle cells do not attach directly to the microstructures of the valves but utilize a tendon cell layer. The myostracum is secreted during the strong shell-adductor muscle attachment that impedes the mantle from controlling crystal growth biologically. This is caused by collagenous fibres that enter myostracal prisms and prevent direct contact between the mantle and myostracal hard tissue. For most bivalves, the myostracum comprises a specific aragonite arrangement with high hardness and prisms that are parallel to adductor muscle fibres. For the development of the latter two characteristics, two crystal growth processes are utilized: (i) *epitactic nucleation* for acquisition of microstructure and texture of the valve template (not the carbonate phase, e.g. [117]) and (ii) *competitive growth* for adjusting crystal face and c-axes orientation normal to inner shell surface, and to secure that large crystals seam inner shell surfaces. The prismatic myostracal microstructure facilitates the attachment and insertion of collagen-rich tendon cell fibrils, which in turn, are connected basally to the tendon cells of the muscles by intracellular action filaments.

6. *Chama* and *Glycymeris* shells are twinned in crossed-lamellar, complex crossed-lamellar as well as myostracal layers. The extent and type of twinning are different for valve and myostracal aragonite. The crossed-lamellar microstructure exhibits polysynthetic twinning between third-order lamellae and cyclic twinning between the first-order lamellae. The myostracum shows cyclic twinning and revokes the polysynthetic restrictions imposed by the crossed-lamellar layer. The complex crossed-lamellar layer exhibits the highest amount of relative twinning frequency and features mostly polycyclic twins within first-order lamellae.

7. Through its specific microstructure resulting from adductor muscle attachment, the myostracum exhibits outstanding physical properties. For *Chama* and *Glycymeris*, the hardness of the valves and myostracum differs by up to 20 %. The average value of respective indentation moduli in valve and myostracum is similar across *Glycymeris* shells, is, however, slightly different for *Chama*. For the latter species, it is always lower than the non-biological reference.

CRediT authorship contribution statement

S. Hoerl: Investigation, Methodology, Visualization, Writing – original draft, Writing – review & editing, Conceptualization, Data curation. **T. le Moine:** Investigation, Visualization, Conceptualization. **N.J. Peter:** Methodology, Writing – review & editing, Data curation. **S. Amini:** Methodology, Writing – review & editing, Data curation. **E. Griesshaber:** Investigation, Writing – original draft, Writing – review & editing, Conceptualization, Supervision. **J. Wang:** Methodology. **E.M. Harper:** Resources, Writing – review & editing. **C. Salas:** Resources, Writing – review & editing. **A.G. Checa:** Formal analysis, Writing – original draft, Writing – review & editing. **R. Schwaiger:** Methodology, Writing – review & editing. **W.W. Schmahl:** Funding acquisition, Project administration, Supervision, Writing – review & editing.

Declaration of competing interest

The authors declare that they have no known competing financial interests or personal relationships that could have appeared to influence the work reported in this paper.

Acknowledgments

Supplementary materials

Supplementary material associated with this article can be found, in the online version, at doi:10.1016/j.mtla.2024.102149.

References

[1] P.Y. Chen, J. McKittrick, M.A. Meyers, Biological materials: functional adaptations and bioinspired designs, Prog. Mater. Sci. 57 (2012) 1492–1704, https://doi.org/10.1016/j.pmatsci.2012.03.001.

[2] H.K. Raut, A.F. Schwartzman, R. Das, F. Liu, L. Wang, C.A. Ross, J.G. Fernandez, Tough and strong: crossed-lamella design imparts multifunctionality to biomimetic nacre, ACS Nano 14 (2020) 9771–9779, https://doi.org/10.1021/acsnano.0c01511.

[3] P. Mohammadi, J. Gandier, W.Wagermaier Nonappa, A. Miserez, M. Penttilä, Bioinspired functionally graded composite assembled using cellulose nanocrystals and genetically engineered proteins with controlled biomineralization, Adv. Mater. 33 (2021) 2102658, https://doi.org/10.1002/adma.202102658.

[4] H. Zhao, S. Liu, X. Yang, L. Guo, Role of inorganic amorphous constituents in highly mineralized biomaterials and their imitations, ACS Nano 16 (2022) 17486–17496, https://doi.org/10.1021/acsnano.2c05262.

[5] S.M. Stanley, Adaptive themes in the evolution of the Bivalvia (Mollusca), Annu. Rev. Earth Planet. Sci. 3 (1975) 361–385, https://doi.org/10.1146/annurev.ea.03.050175.002045.

[6] K.R. Brom, K. Szopa, Morphological diversity of microstructures occurring in selected recent bivalve shells and their ecological implications, Contemp. Trends Geosci. 5 (2016) 104–112, https://doi.org/10.1515/ctg-2016-0008.

[7] Y. Chen, Y. Feng, J.G. Deveaux, M.A. Masoud, F.S. Chandra, H. Chen, D. Zhang, L. Feng, Biomineralization forming process and bio-inspired nanomaterials for biomedical application: a review, Minerals 9 (2019) 68, https://doi.org/10.3390/min9020068.

[8] N.M. Alves, I.B. Leonor, H.S. Azevedo, R.L. Reis, J.F. Mano, Designing biomaterials based on biomineralization of bone, J. Mater. Chem. 20 (2010) 2911, https://doi.org/10.1039/b910960a.

[9] A.R. Studart, Towards high-performance bioinspired composites, Adv. Mater. 24 (2012) 5024–5044, https://doi.org/10.1002/adma.201201471.

[10] S. Yao, B. Jin, Z. Liu, C. Shao, R. Zhao, X. Wang, R. Tang, Biomineralization: from material tactics to biological strategy, Adv. Mater. 29 (2017) 1605903, https://doi.org/10.1002/adma.201605903.

[11] P. Venier, M. Gerdol, S. Domeneghetti, N. Sharma, A. Pallavicini, U. Rosani, A. C. Smaal, J.G. Ferreira, J Grant, J.K. Petersen, Ø. Strand, Biotechnologies from marine bivalves. Goods and Services of Marine Bivalves, Springer International Publishing, Cham, 2019, pp. 95–112, https://doi.org/10.1007/978-3-319-96776-9_6.

[12] S. Tang, Z. Dong, X. Ke, J. Luo, J. Li, Advances in biomineralization-inspired materials for hard tissue repair, Int. J. Oral Sci. 13 (2021) 42, https://doi.org/10.1038/s41368-021-00147-z.

[13] Y. Wang, Q. Liu, Z.F. Lan, B. Zhang, H.Q. Zhang, J.W. Liu, F. Ye, Strong and tough bioinspired nacre-like B4C/Al functionally graded materials with eliminated abrupt interfaces, Compos. Commun. 25 (2021) 100741, https://doi.org/10.1016/j.coco.2021.100741.

[14] Z. Zhang, L. Zhang, C. Li, X. Xie, G. Li, Z. Hu, S. Li, Research progress of chitosan-based biomimetic materials, Mar. Drugs 19 (2021) 372, https://doi.org/10.3390/md19070372.

[15] H. Nakahara, M. Kakei, G. Bevelander, Fine structure and amino acid composition of the organic & in the prismatic layer of some bivalve shells, Venus (Jap. J. Malac.) 39 (1980) 167-177. 10.18941/venusjjm.39.3_167.

[16] G.D. Rosenberg, W.W. Hughes, A metabolic model for the determination of shell composition in the bivalve mollusc, *Mytilus edulis*, Lethaia 24 (1991) 83–96, https://doi.org/10.1111/j.1502-3931.1991.tb01182.x.

[17] I. Kobayashi, T. Samata, Bivalve shell structure and organic matrix, Mater. Sci. Eng. C 26 (2006) 692–698, https://doi.org/10.1016/j.msec.2005.09.101.

[18] J.D. Currey, A.J. Kohn, Fracture in the crossed-lamellar structure of *Conus* shells, J. Mater. Sci. 11 (1976) 1615–1623, https://doi.org/10.1007/BF00737517.

[19] Z. Huang, Z. Pan, H. Li, Q. Wei, X. Li, Hidden energy dissipation mechanism in nacre, J. Mater. Res. 29 (2014) 1573–1578, https://doi.org/10.1557/jmr.2014.179.

[20] I. Almagro, P. Drzymała, K. Berent, C.I. Sainz-Díaz, M.G. Willinger, A. Bonarski, A. G. Checa, New crystallographic relationships in biogenic aragonite: the crossed-lamellar microstructures of mollusks, Cryst. Growth Des. 16 (2016) 2083–2093, https://doi.org/10.1021/acs.cgd.5b01775.

[21] X.Y. Chan, C. Chua, S. Tan, H.Le Ferrand, Energy dissipation in composites with hybrid nacre-like helicoidal microstructures, Compos. B Eng. 232 (2022) 109608, https://doi.org/10.1016/j.compositesb.2021.109608.

[22] W.F. Ponder, D.R. Lindberg, J.M. Ponder, Biology and Evolution of the Mollusca, Volume 1, CRC Press, 2019.

[23] J.D. Taylor, W.J. Kennedy, A. Hall, The shell structure and mineralogy of the Bivalvia Introduction. Nuculacea—Trigonacea, Bull. Br. Mus. Nat. Hist., Zool. (1969) 1–125. Suppl.

[24] Z. Liao, L. Bao, M. Fan, P. Gao, X. Wang, C. Qin, X. Li, In-depth proteomic analysis of nacre, prism, and myostracum of *Mytilus* shell, J. Proteom. 122 (2015) 26–40, https://doi.org/10.1016/j.jprot.2015.03.027.

[25] G. Crippa, E. Griesshaber, A.G. Checa, E.M. Harper, M. Simonet Roda, W. W. Schmahl, Orientation patterns of aragonitic crossed-lamellar, fibrous prismatic and myostracal microstructures of modern *Glycymeris* shells, J. Struct. Biol. 212 (2020) 107653, https://doi.org/10.1016/j.jsb.2020.107653.

[26] G. Crippa, E. Griesshaber, A.G. Checa, E.M. Harper, M. Simonet Roda, W. W. Schmahl, SEM, EBSD, laser confocal microscopy and FE-SEM data from modern *Glycymeris* shell layers, Data Br. 33 (2020) 106547, https://doi.org/10.1016/j.dib.2020.106547.

[27] J.D. Castro-Claros, A. Checa, C. Lucena, J.R. Pearson, C. Salas, Shell-adductor muscle attachment and Ca²⁺ transport in the bivalves *Ostrea stentina* and *Anomia ephippium*, Acta Biomater. 120 (2021) 249–262, https://doi.org/10.1016/j.actbio.2020.09.053.

[28] R.D.K. Thomas, Functional morphology, ecology, and evolutionary conservatism in the Glycymerididae (Bivalvia), Palaeontology 18 (1975) 217–254.

[29] R.R. Vance, A mutualistic interaction between a sessile marine clam and its epibionts, Ecology 59 (1978) 679–685, https://doi.org/10.2307/1938770.

[30] P.G. Oliver, A.M. Holmes, The Arcoidea (Mollusca: bivalvia): a review of the current phenetic-based systematics, Zool. J. Linn. Soc. 148 (2006) 237–251, https://doi.org/10.1111/j.1096-3642.2006.00256.x.

[31] M.C. Carter, *Glycymeris Glycymeris* Dog cockle, Marine Biological Association of the United Kingdom, Plymouth, 2008. https://www.marlin.ac.uk/species/detail/1941.

[32] G. Poppe, Y. Goto. European seashells, volume II (Scaphopoda, bivalvia, cephalopoda), Christa Hemmen, Wiesbaden, 1993, pp. 1–221.

[33] M. Legac, M. Hrs-Brenko, A review of bivalve species in the eastern Adriatic Sea. III. Pteriomorpha (Glycymeridae), Nat. Croat. 8 (1999) 9–25.

[34] R.D.K. Thomas, Shell form and the ecological range of living and extinct Arcoida, Paleobiology 4 (1978) 181–194.

[35] A. Koller-Hodac, D.P. Germann, A. Gilgen, K. Dietrich, M. Hadorn, W. Schatz, P. Eggenberger Hotz, Actuated bivalve robot study of the burrowing locomotion in sediment, in: Proceedings of the 2010 IEEE International Conference on Robotics and Automation, IEEE, 2010, pp. 1209–1214, https://doi.org/10.1109/ROBOT.2010.5509329.

[36] E. Krylova, Bivalves of seamounts of the north-eastern Atlantic. Biogeography of the North Atlantic Seamounts, KMK Scientific Press, Ltd, Moscow, 2006, pp. 76–95.

[37] A.F. Skinner, N. Weicker, ESR dating of *Chione cancellata* and *Chama sinuosa*, Quat. Sci. Rev. 11 (1992) 225–229, https://doi.org/10.1016/0277-3791(92)90067-I.

[38] F.R. Bernard, Living Chamidae of the eastern pacific (Bivalve: heterdonta), Contrib. Sci. 278 (1976) 1–43, https://doi.org/10.5962/p.214207.

[39] W.J. Kennedy, J.D. Taylor, A. Hall, Environmental and biological controls on bivalve shell mineralogy, Biol. Rev. 44 (1969) 499–530, https://doi.org/10.1111/j.1469-185X.1969.tb00610.x.

[40] W.J. Kennedy, N.J. Morris, J.D. Taylor, The shell structure, mineralogy and relationships of the Chamacea (Bivalvia), Paleontology 13 (1970) 379–413.

[41] M. Yonge, Form, habit and evolution in the Chamidae (Bivalvia) with reference to conditions in the rudists (Hippuritacea), Philos. Trans. R. Soc. Lond. B Biol. Sci. 252 (1967) 49–105.

[42] A. Matsukuma, N. Hamada, P.H. Scott, Chama pulchella (Bivalvia : heterodonta) with transposed shell and normal dentition, Venus (Jap. J. Malac.) 56 (1997) 221-231, 10.18941/venusjjm.56.3_221.

[43] J.A. Allen, On the biology and functional morphology of *Chama gryphoides* Linne (Bivalvia; Chamidae), Vie Milieu XXVI (1976) 243–260.

[44] D. Nicol, Nomenclatural review of genera and subgenera of Chamidae, J. Wash. Acad. Sci. 42 (1952) 154–156.

[45] A.A. Berezovsky, Redescription of *Chama clavaticostata* Klushnikov (Bivalvia) from the Middle Eocene of Ukraine, Paleontol. J. 55 (2021) 272–276, https://doi.org/10.1134/S0031030121030072.

[46] G.R. Anstis, P. Chantikul, B.R. Lawn, D.B. Marshall, A critical evaluation of indentation techniques for measuring fracture toughness: I, Direct crack measurements, J. Am. Ceram. Soc. 64 (1981) 533–538, https://doi.org/10.1111/j.1151-2916.1981.tb10320.x.

[47] W.C. Oliver, G.M. Pharr, An improved technique for determining hardness and elastic modulus using load and displacement sensing indentation experiments, J. Mater. Res. 7 (1992) 1564–1583, https://doi.org/10.1557/JMR.1992.1564.

[48] A.J. Schwartz, M. Kumar, B.L. Adams, D.P. Field, Electron Backscatter Diffraction in Materials Science, Springer US, Boston, MA, 2009, https://doi.org/10.1007/978-0-387-88136-2.

[49] T. Hahn, H. Klapper, Twinning of crystals, in: A. Authier (Ed.), International Tables for Crystallography, 1st ed., International Union of Crystallography, Chester, England, 2006, pp. 393–448, https://doi.org/10.1107/97809553602060000644.

[50] E. Griesshaber, W.W. Schmahl, H.S. Ubhi, J. Huber, F. Nindiyasari, B. Maier, A. Ziegler, Homoepitaxial meso- and microscale crystal co-orientation and organic matrix network structure in *Mytilus edulis* nacre and calcite, Acta Biomater. 9 (2013) 9492–9502, https://doi.org/10.1016/j.actbio.2013.07.020.

[51] T. Kogure, M. Suzuki, H. Kim, H. Mukai, A.G. Checa, T. Sasaki, H. Nagasawa, Twin density of aragonite in molluscan shells characterized using X-ray diffraction and transmission electron microscopy, J. Cryst. Growth 397 (2014) 39–46, https://doi.org/10.1016/j.jcrysgro.2014.03.029.

[52] J.G. Carter, Skeletal Biomineralization: Patterns, Processes and Evolutionary Trends: Volume I, Springer, 1990.

[53] S. Hoerl, E. Griesshaber, A.G. Checa, W.W. Schmahl, The diversity in biocrystal morphology and arrangement of Chamide bivalve shells, Crystals 8 (2024), submitted.

[54] A.J. Goetz, D.R. Steinmetz, E. Griesshaber, S. Zaefferer, D. Raabe, K. Kelm, S. Irsen, A. Sehrbrock, W.W. Schmahl, Interdigitating biocalcite dendrites form a 3-D jigsaw structure in brachiopod shells, Acta Biomater. 7 (2011) 2237–2243, https://doi.org/10.1016/j.actbio.2011.01.035.

[55] J. Lastam, E. Griesshaber, X. Yin, U. Rupp, I. Sánchez-Almazo, M. Heß, P. Walther, A. Checa, W. Schmahl, The unique fibrilar to platy nano-and microstructure of twinned rotaliid foraminiferal shell calcite, Sci. Rep. 13 (2023) 2189, https://doi.org/10.1038/s41598-022-25082-9.

[56] N. Wilmot, D. Barber, J. Taylor, A. Graham, Electron microscopy of molluscan crossed-lamellar microstructure, Philos. Trans. R. Soc. Lond. B Biol. Sci. 337 (1992) 21–35.

[57] Í. Almagro, P. Drzymała, A.B. Rodríguez-Navarro, C.I. Sainz-Díaz, M.G. Willinger, J. Bonarski, A.G. Checa, Crystallography and textural aspects of crossed lamellar layers in Arcidae (Bivalvia, Mollusca) shells, KEM 672 (2016) 60–70, https://doi.org/10.4028/www.scientific.net/KEM.672.60.

[58] P. Chantler, Biochemical and Structural Aspects of Molluscan muscle, in: The Mollusca, Elsevier, 1983, pp. 77–154.

[59] S.M. Stanley, Adaptive morphology of the shell in bivalves and gastropods, in: E. R. Trueman, M.R. Clarke (Eds.), The Mollusca, Form and Function, Vol 11, Academic Press, San Diego, 1988, pp. 105–141.

[60] W.M. Kier, The arrangement and function of molluscan muscle, in: E.R. Trueman, M.R. Clarke (Eds.), The Mollusca, Form and Function, Vol 11, Academic Press, San Diego, 1988, pp. 211–252.

[61] H.E. Guderley, I. Tremblay, Swimming in scallops. Developments in Aquaculture and Fisheries Science, Elsevier, 2016, pp. 535–566, https://doi.org/10.1016/B978-0-444-62710-0.00012-2.

[62] J. Bowden, The structure and innervation of lamellibranch muscle. International Review of Cytology, Elsevier, 1958, pp. 295–335.

[63] B.M. Millman, Mechanisms of contraction in molluscan muscle, Am. Zool. 7 (1967) 583–591.

[64] J.C. Rüegg, Smooth muscle tone, Physiol. Rev. 51 (1971) 201–248.

[65] J. Zange, H.O. Pörtner, M.K. Grieshaber, The anaerobic energy metabolism in the anterior byssus retractor muscle of *Mytilus edulis* during contraction and catch, J. Comp. Physiol. B 159 (1989) 349–358, https://doi.org/10.1007/BF00691515.

[66] N. Odintsova, V. Dyachuk, A. Karpenko, Development of the muscle system and contractile activity in the mussel *Mytilus trossulus* (Mollusca, Bivalvia), Russ. J. Dev. 38 (2007) 190–196, https://doi.org/10.1134/S1062360407030071.

[67] N. Odintsova, V. Dyachuk, K. Kiselev, N. Shelud'ko, Expression of thick filament proteins during ontogenesis of the mussel *Mytilus trossulus* (Mollusca: bivalvia), Comp. Biochem. Physiol. B Biochem. Mol. Biol. 144 (2006) 238–244, https://doi.org/10.1016/j.cbpb.2006.03.002.

[68] J.D. Taylor, W.J. Kennedy, The shell structure and mineralogy of *Chama pellucida* Broderip, Veliger 11 (1969) 391–398, pls. 61–64.

[69] A.G. Checa, Physical and biological determinants of the fabrication of molluscan shell microstructures, Front. Mar. Sci. 5 (2018) 353, https://doi.org/10.3389/fmars.2018.00353.

[70] W.W. Schmahl, E. Griesshaber, R.D. Neuser, A. Goetz, C. Lüter, Electron backscatter diffraction study of brachiopod shell calcite – microscale phase and texture analysis of a polycrystalline biomaterial, Part. Part. Syst. Charact. 25 (2008) 474–478, https://doi.org/10.1002/ppsc.200800014.

[71] A.J. Goetz, E. Griesshaber, R.D. Neuser, C. Lüter, M. Hühner, E. Harper, W. W. Schmahl, Calcite morphology, texture and hardness in the distinct layers of rhynchonelliform brachiopod shells, Eur. J. Mineral. 21 (2009) 303–315, https://doi.org/10.1127/0935-1221/2009/0021-1922.

[72] K. Stevens, E. Griesshaber, W. Schmahl, L.A. Casella, Y. Iba, J. Mutterlose, Belemnite biomineralization, development, and geochemistry: the complex rostrum of *Neohibolites minimus*, Palaeogeogr. Palaeoclimatol. Palaeoecol. 468 (2017) 388–402, https://doi.org/10.1016/j.palaeo.2016.12.022.

[73] A.G. Checa, F. Linares, C. Grenier, E. Griesshaber, A.B. Rodríguez-Navarro, W. W. Schmahl, The argonaut constructs its shell via physical self-organization and coordinated cell sensorial activity, iScience 24 (2021), https://doi.org/10.1016/j.isci.2021.103288.

[74] J. Lastam, E. Griesshaber, X. Yin, U. Rupp, I. Sánchez-Almazo, M. Heß, P. Walther, A. Checa, W. Schmahl, Patterns of crystal organization and calcite twin formation in planktonic, rotaliid, foraminifera shells and spines, J. Struct. Biol. 215 (2023) 107898, https://doi.org/10.1016/j.jsb.2022.107898.

[75] S. Hoerl, E. Griesshaber, W.W. Schmahl, Deviations in myostracal microstructures from the competitive growth crystal assembly model in bivalve shells:, *Mytilus edulis, Arctica islandica, Venus verrucosa* and *Tellina planata*, manuscript to be submitted in, Mar. Biol. (2024).

[76] J. Hudson, The microstructure and mineralogy of the shell of a Jurassic mytilid (Bivalvia), Palaeontology 11 (1968).

[77] K. Nishida, R. Nakashima, R. Majima, Y. Hikida, Ontogenetic changes in shell microstructures in the cold seep-associated Bivalve, *Conchocele bisecta* (Bivalvia: thyasiridae), Paleontol. Res. 15 (2011) 193–212, https://doi.org/10.2517/1342-8144-15.4.193.

[78] C. Zhao, L. Ren, Q. Liu, T. Liu, Morphological and confocal laser scanning microscopic investigations of the adductor muscle-shell interface in scallop: morphological and CLSM investigations, Microsc. Res. Tech. 78 (2015) 761–770, https://doi.org/10.1002/jemt.22537.

[79] M.A. Moynihan, S. Amini, N.F. Goodkin, J.T.I. Tanzil, J.Q.I. Chua, G.N. Fabbro, T. Y. Fan, D.N. Schmidt, A. Miserez, Environmental impact on the mechanical properties of *Porites* spp. corals, Coral Reefs 40 (2021) 701–717, https://doi.org/10.1007/s00338-021-02064-3.

[80] Y.A. Shin, S. Yin, X. Li, S. Lee, S. Moon, J. Jeong, M. Kwon, S.J. Yoo, Y.M. Kim, T. Zhang, Nanotwin-governed toughening mechanism in hierarchically structured biological materials, Nat. Commun. 7 (2016) 10772.

[81] J. Wang, X. Zhang, Twinning effects on strength and plasticity of metallic materials, MRS Bull. 41 (2016) 274–281, https://doi.org/10.1557/mrs.2016.67.

[82] L. Zhang, Q. Wang, W. Liao, W. Guo, B. Ye, W. Li, H. Jiang, W. Ding, Effects of cyclic extrusion and compression on the microstructure and mechanical properties of AZ91D magnesium composites reinforced by SiC nanoparticles, Mater. Charact. 126 (2017) 17–27, https://doi.org/10.1016/j.matchar.2017.01.008.

[83] P. Uttam, V. Kumar, K.H. Kim, A. Deep, Nanotwinning: generation, properties, and application, Mater. Des. 192 (2020) 108752.

[84] A.A. Salem, S.R. Kalidindi, R.D. Doherty, S.L. Semiatin, Strain hardening due to deformation twinning in α-titanium: mechanisms, Metall. Mater. Trans. A 37 (2006) 259–268, https://doi.org/10.1007/s11661-006-0171-2.

[85] K. Renard, P.J. Jacques, On the relationship between work hardening and twinning rate in TWIP steels, Mater. Sci. Eng. A 542 (2012) 8–14, https://doi.org/10.1016/j.msea.2012.01.123.

[86] Q. Huang, D. Yu, B. Xu, W. Hu, Y. Ma, Y. Wang, Z. Zhao, B. Wen, J. He, Z. Liu, Y. Tian, Nanotwinned diamond with unprecedented hardness and stability, Nature 510 (2014) 250–253, https://doi.org/10.1038/nature13381.

[87] M. Ding, T. Wang, B. Maerz, S. Robertson, Z. Sun, L. Fan, Y. Shi, H. Wu, Formation of twins in AlON material and its effects on the Vickers hardness and fracture toughness, Ceram. Int. 45 (2019) 21127–21135, https://doi.org/10.1016/j.ceramint.2019.07.089.

[88] S. Amini, A. Masic, L. Bertinetti, J.S. Teguh, J.S. Herrin, X. Zhu, H. Su, A. Miserez, Textured fluorapatite bonded to calcium sulphate strengthen stomatopod raptorial appendages, Nat. Commun. 5 (2014), https://doi.org/10.1038/ncomms4187.

[89] P. Gilbert, A. Lew, C. Stifler, A. Tits, C. Schmidt, E. Luffey, A. Scholl, A. Cantamessa, L. Muller, Y. Delaunois, P. Compère, D. Ruffoni, M. Buehler, Convergent, slightly misoriented crystals toughen corals and seashells, (2022), preprint (version 1), https://doi.org/10.21203/rs.3.rs-1879515/v1.

[90] S. Hoerl, Dependency Between Crystal Organization and Material Properties in Bivalve Shells, Ludwig-Maximilians-Universität, 2022. Master's Thesis.

[91] B. Hubendick, On the molluscan adhesive epithelium, Ark. Zool. (1958) 31–36.

[92] H. Nakahara, G. Bevelander, An electron microscope study of the muscle attachment in the mollusc *Pinctada radiata*, Tex. Rep. Biol. 28 (1970) 279–286.

[93] A.S. Tompa, N. Watabe, Ultrastructural investigation of the mechanism of muscle attachment to the gastropod shell, J. Morphol. 149 (1976) 339–351, https://doi.org/10.1002/jmor.1051490304.

[94] B. Plesch, Shell attachment in the pond snail *Lymnaea stagnalis* (L.), Cell Tissue Res. 171 (1976) 389–396.

[95] S. Isaji, T. Kase, K. Tanabe, K. Uchiyama, Ultrastructure of muscle-shell attachment in *Nautilus pompilius* Linnaeus (Mollusca: cephalopoda), Veliger 45 (2002) 316–330.

[96] G.A. Kahler, F.M. Fisher Jr, R.L. Sass, The chemical composition and mechanical properties of the hinge ligament in bivalve molluscs, Biol. Bull. 151 (1976) 161–181.

[97] M. Yonge, Significance of the ligament in the classification of the Bivalvia, Proc. R. Soc. B 202 (1978) 231–248.

[98] J. Trotter, Functional morphology of force transmission in skeletal muscle: a brief review, Cells Tissues Organs 146 (1993) 205–222.

[99] I. Tremblay, M. Samson-Dô, H.E. Guderley, When behavior and mechanics meet: scallop swimming capacities and their hinge ligament, J. Shellfish Res. 34 (2015) 203–212, https://doi.org/10.2983/035.034.0201.

[100] T. le Moine, Characterization of the Microstructure and the Texture of Calcium Carbonate Crystals in Bivalve shells, Ludwig-Maximilians-Universität, 2022. Master's Thesis.

[101] A. Sancho Vaquer, E. Griesshaber, A.G. Checa, C. Salas, E.M. Harper, W.W. Schmahl, Carbonate crystal microstructure and shape utilization for the formation of foliated, prismatic, vesicular and chalk calcite in Ostreoidea shells. Abstract for Bivalves - Where are we going? (2024).

[102] E. Lopez, B. Vidal, S. Berland, S. Camprasse, G. Camprasse, C. Silve, Demonstration of the capacity of nacre to induce bone formation by human osteoblasts maintained *in vitro*, Tissue Cell 24 (1992) 667–679.

[103] C. Silve, E. Lopez, B. Vidal, D.C. Smith, S. Camprasse, G. Camprasse, G. Couly, Nacre initiates biomineralization by human osteoblasts maintained *in vitro*, Calcif. Tissue Int. 51 (1992) 363–369.

[104] G. Zhang, A. Brion, A. Willemin, M. Piet, V. Moby, A. Bianchi, D. Mainard, L. Galois, P. Gillet, M. Rousseau, Nacre, a natural, multi-use, and timely biomaterial for bone graft substitution, J. Biomed. Mater. Res. 105 (2017) 662–671, https://doi.org/10.1002/jbm.a.35939.

[105] M. Rousseau, Nacre: A biomineral, a natural biomaterial, and a source of bio-inspiration, in: S. Heuss-Aßbichler, G. Amthauer, M. John (Eds.), Highlights in Applied Mineralogy, De Gruyter, Berlin, 2018: pp. 285–300.

[106] L. Cheng, M. Shahin, R. Cord-Ruwisch, Bio-cementation of sandy soil using microbially induced carbonate precipitation for marine environments, Géotechnique 64 (2014) 1010–1013, https://doi.org/10.1680/geot.14.T.025.

[107] A. Mucci, J.W. Morse, The solubility of calcite in seawater solutions of various magnesium concentration, It= 0.697 m at 25 C and one atmosphere total pressure, Geochim. Cosmochim. Acta 48 (1984) 815–822.

[108] F. Wombacher, A. Eisenhauer, F. Böhm, N. Gussone, M. Regenberg, W.C. Dullo, A. Rüggeberg, Magnesium stable isotope fractionation in marine biogenic calcite and aragonite, Geochim. Cosmochim. Acta 75 (2011) 5797–5818, https://doi.org/10.1016/j.gca.2011.07.017.

[109] I. Donald, P. McMillan, Ceramic-matrix composites, J. Mater. Sci. 11 (1976) 949–972.

[110] G. Eckold, Design and Manufacture of Composite Structures, Woodhead publishing, 1994 [5]J. Trotter, Functional morphology of force transmission in skeletal muscle: A brief review, Cells Tissues Organs. 146 (1993) 205–222.

[111] I. Tremblay, H.E. Guderley, Scallops show that muscle metabolic capacities reflect locomotor style and morphology, Physiol. Biochem. Zool. 87 (2014) 231–244, https://doi.org/10.1086/674107.

[112] I. Tremblay, H.E. Guderley, Possible prediction of scallop swimming styles from shell and adductor muscle morphology, J. Shellfish Res. 36 (2017) 17–30, https://doi.org/10.2983/035.036.0104.

[113] J. Hanson, J. Lowy, Structure and function of the contractile apparatus in the muscles of invertebrate animals, in: Structure and Function of muscle, 1, Academic Press, New York, 1960, pp. 265–335, pages.

[114] S.M. Stanley. Relation of Shell Form to Life Habits of the Bivalvia (Mollusca), Geological Society of America Memoirs, Geological Society of America, 1970, pp. 1–282. https://doi.org/10.1130/MEM125-p1.

[115] A. Ansell, E. Trueman, Burrowing in *Mercenaria mercenaria* (Bivalvia, Veneridae), J. Exp. Biol. 46 (1967) 105–115.

[116] K.D.E. Stokesbury, J.H. Himmelman, Experimental examination of movement of the giant scallop, *Placopecten magellanicus*, Mar. Biol. 124 (1996) 651–660, https://doi.org/10.1007/BF00351046.

[117] K. Saruwatari, T. Matsui, H. Mukai, H. Nagasawa, T. Kogure, Nucleation and growth of aragonite crystals at the growth front of nacres in pearl oyster, *Pinctada fucata*, Biomaterials 30 (2009) 3028–3034, https://doi.org/10.1016/j.biomaterials.2009.03.011.